Water, hydrogen cyanide, carbon monoxide, and dust production from distant comet 29P/Schwassmann-Wachmann 1 [*],[**]

D. Bockelée-Morvan[1], N. Biver[1], C.A. Schambeau[2,3], J. Crovisier[1], C. Opitom[4], M. de Val Borro[5], E. Lellouch[1], P. Hartogh[6], B. Vandenbussche[7], E. Jehin[8], M. Kidger[9], M. Küppers[9], D.C. Lis[10], R. Moreno[1], S. Szutowicz[11], and V. Zakharov[12,1]

[1] LESIA, Observatoire de Paris, Université PSL, Sorbonne Université, Université Paris Cité, CNRS, 5 place Jules Janssen, 92195 Meudon, France
e-mail: dominique.bockelee@obspm.fr
[2] Florida Space Institute, University of Central Florida, 12354 Research Parkway, Partnership 1, Orlando, FL 32826, USA
[3] Department of Physics, University of Central Florida, Orlando, FL 32816, USA
[4] Institute for Astronomy, University of Edinburgh, Royal Observatory, Edinburgh, EH9 3HJ, UK
[5] Astrochemistry Laboratory, Goddard Space Flight Center, NASA, 8800 Greenbelt Rd., Greenbelt, MD 20771, USA
[6] Max-Planck-Institut für Sonnensystemforschung, Justus-von-Liebig-Weg 3, 37077 Göttingen, Germany
[7] Instituut voor Sterrenkunde, Katholieke Universiteit Leuven, Celestijnenlaan 200D, Bus-2410, 3000, Belgium
[8] Space sciences, Technologies & Astrophysics Research (STAR) Institute, University of Liège, Liège, Allée du 6 Août 17, 4000, Belgium
[9] European Space Agency European Space Astronomy Centre, Camino Bajo el Castillo, s/n Urbanización Villafranca del Castillo 28692 Villanueva de la Cañada, Madrid, Spain
[10] Jet Propulsion Laboratory, California Institute of Technology, 4800 Oak Grove Drive, Pasadena, CA, 91109, USA
[11] Centrum Badań Kosmicznych Polskiej Akademii Nauk (CBK PAN), Bartycka 18A, Warszawa 00-716, Poland
[12] INAF - Istituto di Astrofisica e Planetologia Spaziali, Area Ricerca Tor Vergata, Via Fosso del Cavaliere 100, 00133 Rome, Italy

ABSTRACT

Context. 29P/Schwassmann-Wachmann 1 is a distant Centaur/comet, showing persistent CO-driven activity and frequent outbursts.
Aims. We aim to better characterize its gas and dust activity from multiwavelength observations performed during outbursting and quiescent states.
Methods. We used the HIFI, PACS and SPIRE instruments of the *Herschel* space observatory on several dates in 2010, 2011, and 2013 to observe the H_2O 557 GHz and NH_3 573 GHz lines and to image the dust coma in the far-infrared. Observations with the IRAM 30 m telescope were undertaken in 2007, 2010, 2011, and 2021 to monitor the CO production rate through the 230 GHz line, and to search for HCN at 89 GHz. The 70 and 160 μm PACS images were used to measure the thermal flux from the nucleus and the dust coma. Modeling was performed to constrain the size of the sublimating icy grains and to derive the dust production rate.
Results. HCN is detected for the first time in comet 29P (at 5σ in the line area). H_2O is detected as well, but not NH_3. H_2O and HCN line shapes differ strongly from the CO line shape, indicating that these two species are released from icy grains. CO production rates are in the range $(2.9–5.6) \times 10^{28}$ s^{-1} (1400–2600 kg s^{-1}). A correlation between the CO production rate and coma brightness is observed, as is a correlation between CO and H_2O production. The correlation obtained between the excess of CO production and excess of dust brightness with respect to the quiescent state is similar to that established for the continuous activity of comet Hale-Bopp. The measured $Q(H_2O)/Q(CO)$ and $Q(HCN)/Q(CO)$ production rate ratios are 10.0 ± 1.5 % and 0.12 ± 0.03 %, respectively, averaging the April-May 2010 measurements ($Q(H_2O) = (4.1 \pm 0.6) \times 10^{27}$ s^{-1}, $Q(HCN) = (4.8 \pm 1.1) \times 10^{25}$ s^{-1}). We derive three independent and similar values of the effective radius of the nucleus, ∼ 31 ± 3 km, suggesting an approximately spherical shape. The inferred dust mass-loss rates during quiescent phases are in the range 30–120 kg s^{-1}, indicating a dust-to-gas mass ratio < 0.1 during quiescent activity. We conclude that strong local heterogeneities exist on the surface of 29P, with quenched dust activity from most of the surface, but not in outbursting regions.
Conclusions. The volatile composition of the atmosphere of 29P strongly differs from that of comets observed within 3 au from the Sun. The observed correlation between CO, H_2O and dust activity may provide important constraints for the outburst-triggering mechanism.

Key words. Comets: general; Comets: individual: 29P/Schwassmann-Wachmann 1; Radio lines: planetary systems; Infrared: planetary systems

1. Introduction

Comet 29P/Schwassmann-Wachmann 1 is a periodic comet orbiting on a nearly circular orbit with a small inclination ($i = 9.4°$) at 6 au from the Sun. It is also classified as a Centaur, which is a transition object between the trans-neptunian and Jupiter-family dynamical populations. Comet 29P is the most notable occupant of the short-lived dynamical Gateway, a temporary low-eccentricity region exterior to Jupiter through which the majority of Jupiter-family comets pass (Sarid et al. 2019). The properties of its nucleus are poorly constrained. Its size is estimated to be ∼ 30 km in radius (Stansberry et al. 2004; Bauer et al. 2013; Schambeau et al. 2015, 2021).

Comet 29P is well known for its permanent activity and its episodic outbursts, which can change its visual brightness from typically $m_v = 16$ to 11 during major outbursts (e.g. Trigo-Rodríguez et al. 2008, 2010; Miles 2016). The outbursts are observed with some periodicity (about every 57 d), which is thought to correspond to the rotation period of the nucleus, and which suggests that the triggering mechanism involves the insolation of specific regions (Trigo-Rodríguez et al. 2010; Miles 2016). Carbon monoxide is permanently detectable in the coma with a production rate of typically 3–5 × 10^{28} s^{-1}, and is thought to be the main driver of the activity (Senay & Jewitt 1994; Crovisier et al. 1995; Festou et al. 2001; Gunnarsson et al. 2002, 2008; Paganini et al. 2013). Dust outbursts seem not always to be associated with an increase in the CO production (Wierzchos & Womack 2020). In addition to CO, H_2O (in the infrared, Ootsubo et al. 2012) and daughter species CO$^+$, CN, and possibly N$_2^+$ (in the visible, Cochran & Cochran 1991; Korsun et al. 2008; Ivanova et al. 2016) have been detected in comet 29P. At 6 au from the Sun, water sublimation from the nucleus is expected to be very inefficient. The amorphous-to-crystalline water transition phase that may proceed inside the nucleus is thought to be responsible for the outbursts (Prialnik & Bar-Nun 1987, 1990; Enzian et al. 1997; Kossacki & Szutowicz 2013).

We present in this paper observations of 29P obtained in 2010-2013 with the *Herschel* space observatory (Pilbratt et al. 2010) in the framework of the guaranteed-time key programme "Water and related chemistry in the Solar System" (Hartogh et al. 2009), which targeted several comets (e.g. Bockelée-Morvan et al. 2010b; de Val-Borro et al. 2010; Biver et al. 2012; Bockelée-Morvan et al. 2012, 2014; de Val-Borro et al. 2014). Searches for H_2O (557 GHz) and NH$_3$ (573 GHz) lines were performed with the Heterodyne Instrument for the Far-Infrared (HIFI, de Graauw et al. 2010), which led to the first far-infrared detection of water. A previous attempt to detect the 557 GHz H_2O line in comet 29P using the Odin space telescope was unsuccessful (Biver et al. 2007). Continuum images at 70 and 160 μm were obtained using the Photodetector Array Camera and Spectrometer (PACS, Poglitsch et al. 2010), and at 250, 350 and 500 μm with the Spectral and Photometric Imaging REceiver (SPIRE, Griffin et al. 2010). Unlike the PACS observations, those with SPIRE did not lead to a conspicuous detection. We also gather in this paper observations of CO and HCN carried out in 2007, 2010, 2011 and 2021 with the 30 m antenna of the Institut de radioastronomie millimétrique (IRAM), as well as optical photometry observations that place the *Herschel* and IRAM data in context.

The observations are described in Sect. 2. The gas production rates are derived in Sect. 3. Section 4 studies the correlations between production rates and dust activity. In Sect. 5 we present observational evidence for the predominant release of H_2O and

HCN molecules by icy grains in the atmosphere of 29P. The H_2O observations are analyzed with a model simulating the sublimation of icy grains released during an outburst. Section 6 presents an analysis of the nucleus and dust thermal emissions observed with PACS. In Sect. 7 the SPIRE data are discussed. A summary follows in Sect. 8. The models that are used to describe the dynamics, thermal properties, and sublimation of icy grains are presented in the appendix. A preliminary summary of these observations was given by Bockelée-Morvan et al. (2010a).

2. Observations

2.1. HIFI observations
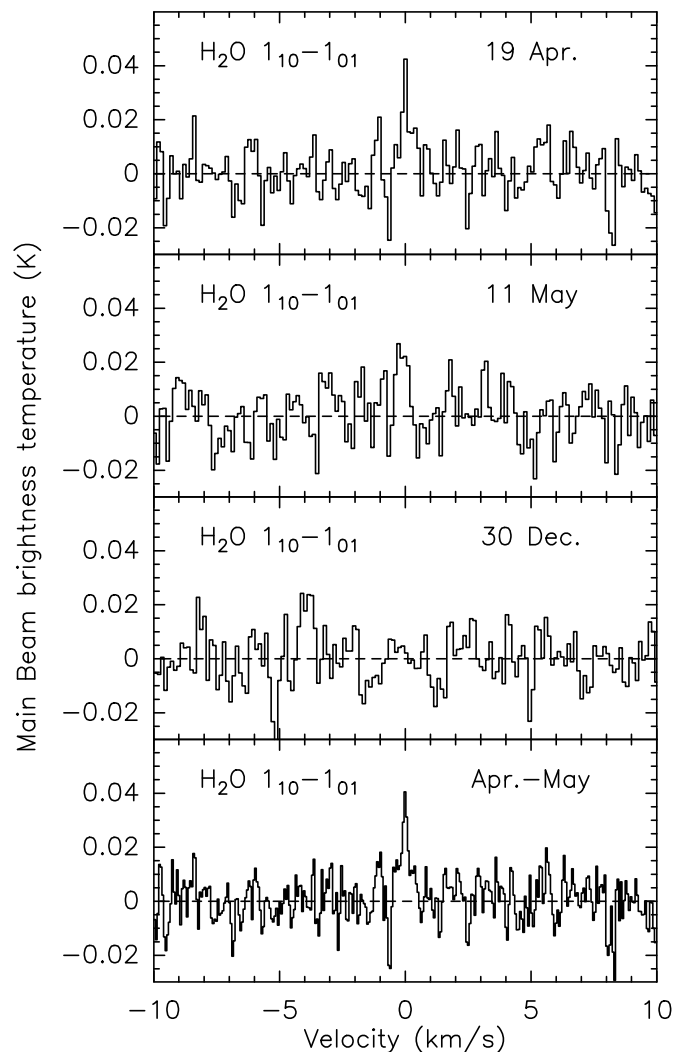
Fig. 1. H_2O $1_{10}-1_{01}$ line observed in comet 29P in 2010 with the HIFI instrument of *Herschel*. The UT date of the observation is indicated in the upper right corner. The velocity scale is in the comet rest frame. The spectra, acquired with the HRS, have been smoothed to a spectral resolution of 129 m s^{-1}, except for the bottom spectrum which shows the average of the spectra obtained on 19 April and 11 May at a spectral resolution of 67 m s^{-1}.

Observations with the *Herschel*/HIFI instrument were performed on 19 April, 11 May, and 30 December 2010, when the comet was at $r_h = 6.2$ au from the Sun. A log of the observations, with the geometrical parameters (heliocentric dis-

Table 1. Log of the *Herschel* observations of 29P.

Date (UT) dd.dd/mm/yyyy	r_h (au)	Δ (au)	Instrument	ObsId	Measurement	Int.[a] (min)	m_R^b	$\Delta T_{outburst}^c$ (day)
19.05/04/2010	6.206	5.814	HIFI	1342195094	H_2O 1_{10}–1_{01}, NH_3 1_0–0_0	59	13.2	3.0(D)
11.02/05/2010	6.210	6.165	HIFI	1342196411	H_2O 1_{10}–1_{01}, NH_3 1_0–0_0	48	15.3	25(D), 5.5(E)
30.24/12/2010	6.244	5.875	HIFI	1342212132	H_2O 1_{10}–1_{01}, NH_3 1_0–0_0	51	16.2	> 81
10.49/06/2010	6.215	6.634	PACS	1342198444/45	Photo 70 & 160 μm	24	16.1	36(E), 17(F)
02.70/01/2011	6.244	5.822	PACS	1342212281/82	Photo 70 & 160 μm	95	16.6	> 84
17.75/02/2013	6.231	5.820	PACS	1342263832-35	Photo 70 & 160 μm	169	16.4	> 42
10.57/06/2010	6.215	6.635	SPIRE	1342198449	Photo 250, 350, & 500 μm	55	16.1	36(E), 17(F)

[a] Integration time. [b] Nuclear *R*-magnitude of comet 29P in a 10″-diameter aperture. [c] Time after the outbursts listed in Table 5 with the label given within the brackets.

Table 2. H_2O 1_{10}–1_{01}, NH_3 1_0–0_0, and HCN $J(1-0)$ line areas and Doppler shifts, together with the gas production rates.

UT date (dd.dd/yyyy)	r_h (au)	Molec.	Line area[a] (mK km s^{-1})	Velocity shift (km s^{-1})	Production rate (s^{-1}) Nucleus[b]	Icy grains[c] $L_p=10^4$ km	Icy grains[c] $L_p= 5\times10^4$ km
19.05/04/2010	6.206	H_2O	19.0 ± 2.9[d]	+0.04 ± 0.04	(4.6±0.8)×10^{27}	(1.6±0.3)×10^{27}	(4.4±0.8)×10^{27}
11.02/05/2010	6.210	H_2O	13.9 ± 3.4[d]	−0.16 ± 0.08	(3.5±0.9)×10^{27}	(1.3±0.3)×10^{27}	(3.5±0.9)×10^{27}
30.24/12/2010	6.244	H_2O	< 9.8[d]	–	<2.4×10^{27}	<0.8×10^{27}	<2.3×10^{27}
19.05/04/2010	6.206	NH_3	< 13	–	<5.6×10^{27}		
11.02/05/2010	6.210	NH_3	< 15	–	<7.1×10^{27}		
30.24/12/2010	6.244	NH_3	< 14	–	<6.0×10^{27}		
30.80/12/2007[e]	5.981	HCN	19 ± 8	–	(3.2±1.3)×10^{25}	(2.7±1.1)×10^{25}	(4.8±2.0)×10^{25}
12.06/02/2010	6.194	HCN	10 ± 10	–	(1.9±1.9)×10^{25}	(1.6±1.6)×10^{25}	(2.9±2.9)×10^{25}
05.00/05/2010[f]	6.210	HCN	21 ± 5	–	(4.8±1.1)×10^{25}	(4.1±0.9)×10^{25}	(7.2±1.7)×10^{25}
11.18/01/2011	6.245	HCN	37 ± 9	–	(8.2±2.0)×10^{25}	(7.0±1.7)×10^{25}	(1.2±0.3)×10^{26}
14.95/11/2021[g]	5.931	HCN	< 18	–	< 3×10^{25}	< 2.6 ×10^{25}	< 4.5 ×10^{25}
Average 2007–2011	6.2	HCN	21 ± 4	−0.04 ± 0.07	(4.4±0.8)×10^{25}	(3.7±0.7)×10^{25}	(6.6±1.2)×10^{25}

Notes. 3-σ upper limits are given in case of non detection. [a] Line area in main-beam brightness temperature scale. For HCN $J(1-0)$, sum of the three hyperfine components. [b] In the assumption of nucleus production, and assuming a coma temperature of 6 K (see Sect. 3.1). [c] In the assumption of production from icy grains at the cometocentric distance L_p, with release at a temperature of 100 K (see Sect. 3.1). [d] Line area measured on HRS spectra. [e] Mean date for the average of measurements performed on 29.8 and 31.8 Dec 2010. [f] Mean date for the average of measurements performed on 17.87 April, 30.79 April, 22.6 May, and 28.78 May 2010. [g] Mean date for the average of measurements performed in November 2021.

tance r_h and the comet-observer distance Δ), is presented in Table 1. The H_2O 1_{10}–1_{01} and NH_3 $1_0 - 0_0$ lines, at 556.9360 and 572.5498 GHz, respectively, were observed simultaneously in the lower and upper sidebands of band 1b of the HIFI receiver. They were observed in the two orthogonal horizontal (H) and vertical (V) polarizations. The observing mode was frequency-switching (FSW) with a frequency throw of 94.5 MHz. Spectra were acquired with both the Wide Band Spectrometer (WBS) and High Resolution Spectrometer (HRS). The spectral resolution of the WBS is 1.1 MHz. The HRS was used in the high-resolution mode (125 kHz spectral resolution corresponding to ~0.07 km s^{-1}). The integration time was typically about 1 h for each measurement (Table 1). The half-power beam width (HPBW) is 38.1″ at 557 GHz (Teyssier et al. 2017). The comet was tracked using the ephemeris from JPL Horizons.

The pointing for *Herschel* observations taken between 30 March 2010 and 14 June 2011 was offset due to a warm star-tracker. As a consequence, the HIFI observations of comet 29P

experienced small pointing offsets. We used HIPE v12.0[1] to calculate the improved pointing corrections using the most accurate representation of the star tracker focal length. We also took the pointing offset between H and V polarisation beams of 6.6″ in band 1b into account (about 20% of the full width at half-maximum of the beam, Teyssier et al. 2017). The largest offset of the comet nucleus corresponds to about 5″ from the center of the synthetic beam; it occurred for the April 2010 H+V average observation. The average pointing offsets for the May 2010 and December 2010 are 3.8 and 3.3″, respectively.

Figure 1 shows the H_2O spectra obtained with the HRS spectrometer, averaging the two polarizations. Intensities are given in units of main-beam brightness temperature, assuming a main-beam efficiency of 0.62, and a forward efficiency of 0.96 (Shipman et al. 2017; Teyssier et al. 2017). H_2O is detected in April and May 2010, with a signal-to-noise ratio of 6.6 and 4.1, respectively. The signal-to-noise ratio in the line area is 7.4, averaging the two periods. When these April and May 2010 data

---

[1] The last version of HIPE was 15.0, but the different versions do not affect the data reduction.

are averaged, the H_2O line is approximately centered at the zero Doppler velocity in the comet rest frame ($\Delta v = -0.08 \pm 0.05$ km s^{-1}), and the line width of the April-May averaged spectrum is 0.48 ± 0.07 km s^{-1}. However, the spectrum obtained on 30 December, 2010 shows no indication of a line. The NH$_3$ $1_0 - 0_0$ line is not detected in any of the observed periods.

Measured line areas, or their upper limits, are given in Table 2. We also provide the mean velocity shift of the line with respect to the comet frame in this table.

2.2. PACS observations

The *Herschel*/PACS imaging observations were obtained on 10 June 2010, that is one to two months after the HIFI measurements of April-May 2010, on 2 January 2011, that is three days after the H_2O observations of December 2010, and on 17 February 2013 (Table 1). In photometer mode, the PACS instrument takes images simultaneously in two of its three filters at 70 μm, 100 μm and 160 μm (red, green, and blue) that cover the 60-85 μm, 85-125 μm, and 125-210 μm ranges, respectively. The maps presented here were taken in the red and blue bands with orthogonal scanning directions with respect to the detector array using the medium-scan slewing speed of 20″/s. For the May 2010 observations, we used three scan legs with a 9.9′ length and a 2.5′ leg separation, while the January 2011 observation have eight scan legs with a 5′ length and 0.3′ leg separation. The mini-scan map mode was used in February 2013 (eight legs with 3′ length and 0.03′ leg separation). The pixel sizes are $6.4'' \times 6.4''$ and $3.2'' \times 3.2''$ for the red and blue channels, respectively. On 17.75 February 2013, one of the two PACS red arrays was not operational (Exter et al. 2018). This issue did not affect the data quality, but the size of the 160 μm image is smaller and the comet is offset from the center of the image.

We downloaded and used Level 2.5 Unimap maps produced by the PACS scan-map pipeline from the Herschel Science Archive[2] (Exter et al. 2018). For the Level 2.5 maps, the blue images were resampled to a pixel scale of 1.6″/pixel and the red images to 3.2″/pixel. The Level 2.5 maps were calibrated to Jy/pixel values and include a local background removal. Additionally, inspection of the Level 2.5 maps beyond the region of coma contributions revealed a low-level residual background from each image that was removed before their analysis.

The PACS 70 μm and 160 μm images are shown in Fig. 2 for the three different epochs. The 70 μm image obtained on 10 June 2010 is more extended than others. This is further discussed in Sect. 6.3.

2.3. SPIRE observations

The *Herschel*/SPIRE imaging observations were undertaken on 10 June 2010, approximately 2 hours after the PACS data acquisition (Table 1). In photometry mode, the SPIRE instrument takes images with fields of view (FOV) of $4' \times 8'$ simultaneously in three filters centered on 250 μm, 350 μm, and 500 μm. 29P was imaged using the small-map mode which involved scanning the telescope across the sky at 30″/s in two nearly orthogonal scan paths. Level 2 scan maps were acquired from the *Herschel* Science Archive. For 29P, the small-scan maps used for analysis were those generated for Solar System objects, consisting of calibrated maps in Jy/beam, corrected for the proper motion of 29P (Valchanov 2017). The Level 2 scan maps have a circular FOV with a radius of ∼ 5′ that includes observational coverage

from each of the individual detector scans. The HPBW of SPIRE photometer is 17.9″, 24.2″, and 35.4″ at 250 μm, 350 μm, and 500μm, respectively.

The SPIRE images are shown in Fig. A.1. A marginal signal is observed at the position of comet 29P, especially in the 250 μm image. However, the images are crowded by signals from astronomic sources with similar or higher intensity.

2.4. IRAM 30 m observations

In support of the *Herschel* observations, comet 29P was observed from the ground at millimeter wavelengths with the IRAM 30 m telescope. We also include in this paper observations undertaken in 2007 and 2021. The log of the observations is presented in Table 3.

Observations in 2007 were performed in frequency-switching mode (FSW; throw of 7.2 MHz) with the A100/B100 and A230/B230 receivers used in parallel. This combination of receivers allowed us to simultaneously observe the HCN J(1–0) and CO J(2–1) lines at 88.632 GHz and 230.538 GHz, respectively, in horizontal and vertical polarizations. Spectra were acquired with the VESPA autocorrelator at a spectral resolution of 20 kHz (66 and 25 m s^{-1}, at 89 and 230 GHz, respectively). This high spectral resolution is needed to resolve the narrow blueshifted peak of the CO line (Fig. 3).

For the observations undertaken in 2010, 2011, and 2021, we used the EMIR front-end, installed at the telescope in 2009. EMIR 230 GHz and 90 GHz receivers were used simultaneously, to observe the CO J(2–1) and HCN J(1–0) lines. Observations in 2010–2011 were undertaken in beam-switching mode (WSW), using the wobbling secondary mirror, with the sky reference position at 3′ from the comet. Those of 2021 were obtained either in WSW, in FSW, or in position-switching mode (PSW) with a reference at 5′. The 2007 data contain spectra observed with VESPA at a spectral resolution of 20 kHz.

The daily integration time was between 12 and 70 min (Table 3). The IRAM HPBW is 10.7″ and 27.8″ at 230 GHz and 89 GHz, respectively. The main-beam efficiency was estimated by observing planets to ∼ 0.73 at 89 GHz and in the range 0.48–0.57 at 230 GHz (depending on the date). The forward efficiency is 0.95 and 0.91 at 89 and 230 GHz, respectively.

The CO J(2–1) line is readily detected on individual days (Fig. 3). This line was first detected in 29P at the James Clerk Maxwell Telescope (JCMT) (Senay & Jewitt 1994). It was then observed numerous times at IRAM, at the Swedish ESO Submillimetre Telescope (SEST), or with the Arizona Radio Observatory 10 m Submillimeter Telescope (SMT) (Crovisier et al. 1995; Festou et al. 2001; Gunnarsson et al. 2002, 2008; Wierzchos & Womack 2020). The CO spectra present the characteristic CO line shape observed in this comet, namely, a blueshifted line (velocity shift $\Delta v = -0.2$ to -0.3 km s^{-1}, Table 4), with a strong and narrow (full width at half maximum of 0.123 ± 0.005 km s^{-1}) peak at $v = -0.5$ km s^{-1}. The high S/N November 2021 spectrum also distinctly shows a peak at +0.25 km s^{-1}.

The HCN J(1–0) line is detected marginally in December 2007, April–May 2010, and January 2011, but not in November 2021. The upper limit for 2021 is consistent with most other measurements (Table 2). When the 2007–2011 data are averaged, the signal to noise ratio is 5.2 in the line area (Table 2, Fig. 4). This is the first detection of HCN in comet 29P. From a Gaussian fit to the main F(2–1) hyperfine component, the width of the line is 0.88 ± 0.41 km s^{-1}. As for water, the HCN line
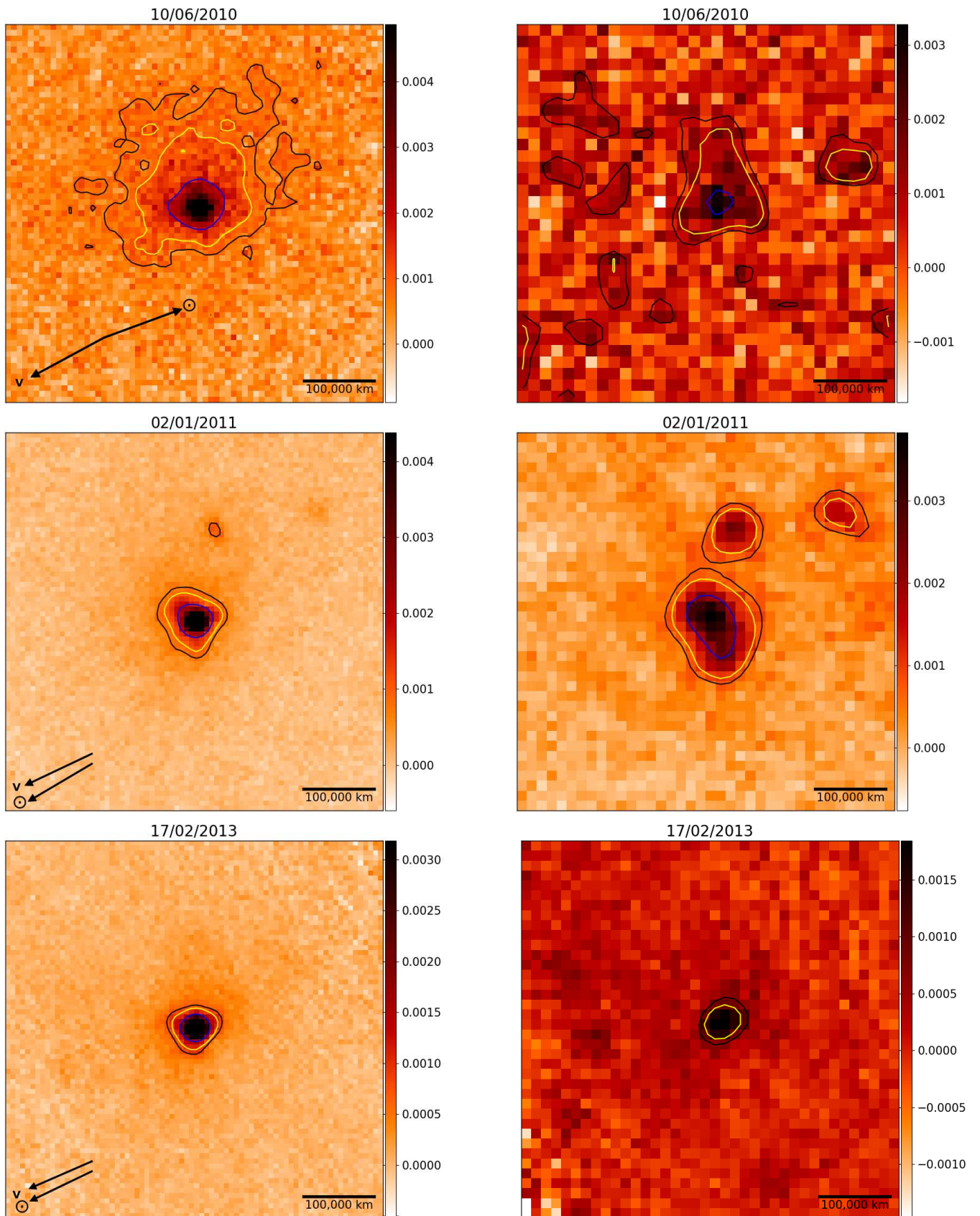
Fig. 2. Cropped PACS images of 29P in the 60-85 μm band (left) and in the 125–210 μm band (right). Dates from top to bottom are 10 June 2010, 2 January 2011, and 17 February 2013. Flux per pixel (1.6 and 3.2″ for the 70 and 160 μm images, respectively) is given in Jy (color bar). The projected skyplane field of view is the same for each image (5.13×10^5 km $\times$ 5.13×10^5 km). Arrows indicate the skyplane-projected Sun direction and comet-projected trajectory. Negative pixel values are the result of the local background subtraction. Comet 29P was in quiescent state at the three dates (Table 1).

Table 3. Log of the IRAM-30m observations of 29P.

Date (UT) dd.dd/mm/yyyy	r_h (au)	Δ (au)	τ^a	Int. (min)	Mode	Lines	m_R^b	$\Delta T^c_{outburst}$ (day)
29.80–29.83/12/2007	5.981	5.009	0.1	42	FSW	CO J(2–1), HCN J(1–0)	15 ± 1^d	0.2(A)
30.80–30.83/12/2007	5.981	5.012	0.1	36	FSW	CO J(2–1)	13.0	1.2(A)
31.81–31.82/12/2007	5.981	5.014	0.07	12	FSW	CO J(2–1), HCN J(1–0)	13.1	2.2(A)
12.04–12.07/02/2010	6.194	5.207	0.08	32	WSW	CO J(2–1), HCN J(1–0)	13.0	9.6(C)
17.84–17.90/04/2010	6.206	5.795	0.4	56	WSW	CO J(2–1), HCN J(1–0)	12.9	1.8(D)
30.74–30.84/04/2010	6.208	5.999	0.57	70	WSW	CO J(2–1), HCN J(1–0)	15.2	15(D)
22.61–22.67/05/2010	6.212	6.347	0.48	66	WSW	CO J(2–1), HCN J(1–0)	15.5	37(D), 17(E)
28.75–28.80/05/2010	6.213	6.442	0.4–1.1	42	WSW	CO J(2–1), HCN J(1–0)	14.7	43(D), 23(E) 4.4(F)
11.16–11.21/01/2011	6.245	5.697	0.22	50	WSW	CO J(2–1), HCN J(1–0)	16.6	> 93
13.92–13.96/11/2021	5.930	5.017	0.24	45	WSW+FSW	CO J(2–1), HCN J(1–0)	16.1	47(G), 21(H) 10(I)
14.92–14.97/11/2021	5.931	5.011	0.10	46	PSW+FSW	CO J(2–1), HCN J(1–0)	16.0	48(G), 22(H) 11(I)
15.98–15.99/11/2021	5.931	5.006	0.08	12	FSW	CO J(2–1), CH$_3$OH J(5–4)	16.1	49(G), 23(H) 12(I)

[a] Atmospheric opacity at 225 GHz. [b] Nuclear red magnitude in a 10″-diameter aperture. [c] Time after outbursts listed in Table 5, with the label given within the brackets. [d] Interpolated from the reported nuclear magnitudes of 15.9 on 28.97 December 2007, and 14.0 on 29.91 December 2007.

Table 4. CO J(2–1) line areas, Doppler shifts, and production rates.

UT date (dd.dd/mm/yyyy)	r_h (au)	Molecule	Line area^a (mK km s^{-1})	Velocity shift (km s^{-1})	Prod. rate^b (s^{-1})	Jet component Prod. rate$^{b,\,c}$ (s^{-1})
29.82/12/2007	5.981	CO	271 ± 18	−0.25 ± 0.03	$(4.8 \pm 0.3) \times 10^{28}$	$(2.6 \pm 0.2) \times 10^{28}$
30.82/12/2007	5.981	CO	301 ± 17	−0.19 ± 0.02	$(5.1 \pm 0.3) \times 10^{28}$	$(2.2 \pm 0.2) \times 10^{28}$
31.81/12/2007	5.981	CO	292 ± 30	−0.26 ± 0.05	$(4.9 \pm 0.5) \times 10^{28}$	$(2.7 \pm 0.3) \times 10^{28}$
12.05/02/2010	6.194	CO	332 ± 9	−0.28 ± 0.01	$(5.6 \pm 0.2) \times 10^{28}$	$(3.4 \pm 0.1) \times 10^{28}$
17.87/04/2010	6.206	CO	265 ± 14	−0.18 ± 0.02	$(4.8 \pm 0.3) \times 10^{28}$	$(2.1 \pm 0.1) \times 10^{28}$
30.79/04/2010	6.208	CO	188 ± 17	−0.36 ± 0.05	$(3.6 \pm 0.3) \times 10^{28}$	$(2.7 \pm 0.2) \times 10^{28}$
22.64/05/2010	6.212	CO	201 ± 18	−0.24 ± 0.04	$(4.0 \pm 0.4) \times 10^{28}$	$(2.2 \pm 0.2) \times 10^{28}$
28.78/05/2010	6.213	CO	189 ± 26	−0.21 ± 0.05	$(3.9 \pm 0.5) \times 10^{28}$	$(1.9 \pm 0.3) \times 10^{28}$
11.18/01/2011	6.245	CO	159 ± 10	−0.27 ± 0.03	$(2.9 \pm 0.2) \times 10^{28}$	$(1.7 \pm 0.1) \times 10^{28}$
13.94/11/2021	5.930	CO	185 ± 10	−0.30 ± 0.03	$(3.0 \pm 0.2) \times 10^{28}$	$(1.9 \pm 0.1) \times 10^{28}$
14.95/11/2021	5.931	CO	201 ± 5	−0.21 ± 0.01	$(3.3 \pm 0.1) \times 10^{28}$	$(1.7 \pm 0.1) \times 10^{28}$
15.99/11/2021	5.931	CO	190 ± 9	−0.20 ± 0.02	$(3.1 \pm 0.2) \times 10^{28}$	$(1.5 \pm 0.1) \times 10^{28}$

Notes. [a] Line area on the main-beam brightness temperature scale. [b] Assuming nucleus production, and a coma temperature of 6 K (see Sect. 3.1). [c] Derived from the line area measured between −0.7 and −0.3 km s^{-1}.

does not present a significant velocity offset ($\Delta v = -0.04 \pm 0.07$ km s^{-1}, Table 2), in contrast to the CO line.

2.5. Context from optical observations

Comet 29P is the target of several photometric monitoring campaigns with the aim to understand the origin of its outbursts. Trigo-Rodríguez et al. (2008) established an outburst frequency of 7.3 outbursts/year. We list in Table 5 relevant outbursts (labeled by letters) that occurred before one of our observations, and their amplitude Δm_R. The elapsed times $\Delta T_{outburst}$ between the outburst time and the HIFI and IRAM observations are given in Tables 1 and 3, respectively. We also provide for each observing date the R magnitude (referred to as the nuclear magnitude) m_R measured within a 10″ diameter aperture (or the visual magnitude in a 13″ diameter aperture which is comparable to m_R),
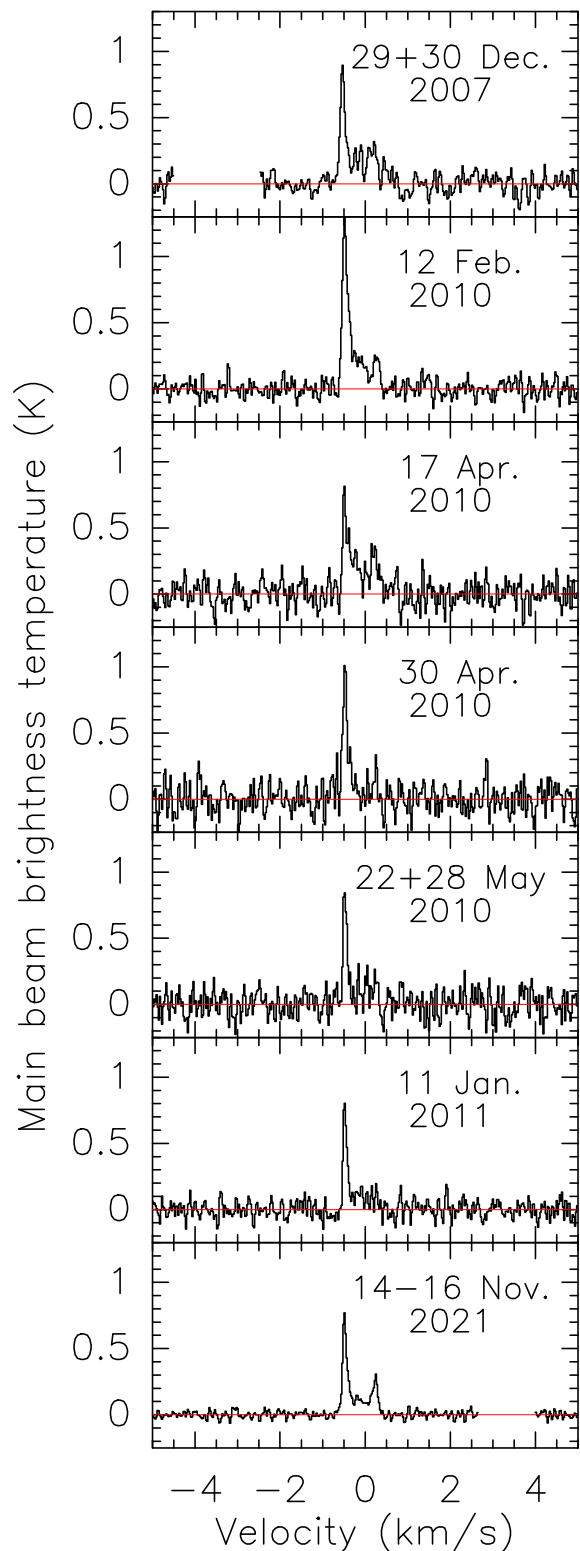
Fig. 3. CO $J(2–1)$ line observed in comet 29P with the IRAM 30 m telescope, from 2007 to 2021. Channels corresponding to the CO line from Earth's mesosphere (2007 spectrum obtained in FSW mode) and CO galactic lines (the 2021 spectrum includes data in PSW mode) are blanked. The velocity scale is in the comet rest frame. The spectral resolution is 51 m s^{-1}.

taken from the LESIA data base[3], Minor Planet Center[4], M.
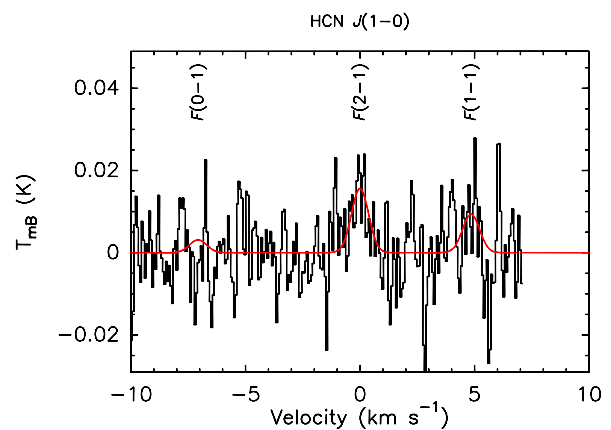
³ https://lesia.obspm.fr/comets

Fig. 4. HCN $J(1–0)$ line observed in comet 29P with the IRAM 30 m telescope, averaging 2007 to 2011 data. A Gaussian fit to the $F(2–1)$ main hyperfine component is shown by the red line. The Gaussian curves centered at the velocity of the $F(0–1)$ and $F(1–1)$ were rescaled assuming statistical weight ratios. The vertical scale is the main-beam brightness temperature. The velocity scale is in the comet rest frame. The spectral resolution is 66 m s^{-1}.

Kidger homepage[5], R. Miles page on British Astronomical Association website[6], and Miles (2016). m_R values at the date of *Herschel* and IRAM observations are given in Tables 1 and 3, respectively.

The PACS continuum observations were obtained during quiescent activity ($m_R \sim 16.4$, Table 1). The first two H$_2$O observations took place 3.0 and 25.0 days after the major outburst of 16.8 April 2010 ($\Delta m_R = 3.9$, outburst D). Two other outbursts (E & F) of small amplitude occurred in May 2010, with outburst E ($\Delta m_R = 1.0$) only 5.5 days before the second observation. As for the third H$_2$O observation on 30 December 2010, the comet was in a quiescent phase since mid-October 2010. In Table 5, we list the outburst (B) of 9.71 November 2009 because H$_2$O was detected with the *Akari* telescope nine days after this relatively faint outburst (Ootsubo et al. 2012).

The CO and HCN observations in December 2007 and February 2010 were obtained close in time to major outbursts A and C, respectively. This is the case especially for the 29.80–29.83 December 2007 data. R. Miles (personal communication) estimates the time of outburst A to 29.42±0.37 December 2007 (updating the value given in Miles (2016)). Using three 29P images from R. Ligustri[7] obtained on 31.778 December 2007, 1.833 January 2008, and 8.842 January 2008, we have estimated the outburst time from the expanding shell to $29.61^{+0.3}_{-0.5}$ December 2007 (with an expansion rate of 0.154 km s^{-1}). The resulting elapsed time $\Delta T_{\mathrm{outburst}}$ between outburst A and the first CO December 2007 observation is in the range [–0.1 d, 0.7 d] with a central value at +0.2 d.

The comet was quiescent at the time of the January 2011 CO and HCN observations. The November 2021 observations were conducted about one month and a half after its major outburst of 27.8 September 2021 ($\Delta m_R = 4.5$, outburst G). Outbursts are also reported for 16.88 October ($\Delta m_R = 0.35$), 23.75 October ($\Delta m_R = 2.5$, outburst H) and 3.4 November 2021 ($\Delta m_R = 0.6$, outburst I). However, 29P was back to a quiescent state when observed at IRAM on 14 to 16 November 2021 ($m_R \sim 16$, Table 3).

⁴ https://minorplanetcenter.net/db_search
⁵ http://www.observadores-cometas.com/
⁶ https://britastro.org/node/25120
⁷ Available on S. Yoshida home page http://www.aerith.net/

To study how the gas production rates correlate with dust activity (see Sect. 4), we corrected the apparent magnitude m_R ($= m_R(\Delta, r_h, \theta)$) for the geocentric distance and phase angle θ according to

$$m_R(1, r_h, 0) = m_R(\Delta, r_h, \theta) - 5\log_{10}(\Delta) + 2.5\log_{10}(\phi[\theta]), \qquad (1)$$

where $\phi(\theta)$ is the phase function normalized to $\phi = 0°$ from Schleicher & Bair (2011). Admittedly, this is not the most appropriate geocentric correction as the magnitude is measured in a fixed angular aperture. In addition, a heliocentric correction should be considered to take into account the r_h^{-2} dependence of the solar light scattering on the dust particles. Since the spanned ranges of r_h and Δ are small along the orbit of 29P, we nonetheless used the commonly used correction given in Eq. 1.

Table 5. Relevant 29P outbursts.

Outburst date		Peak m_R	Δm_R	Ref.	Label
$29.61^{+0.3}_{-0.5}$	Dec 2007	12.7	3.4	(1, 2)	A
9.71 ± 0.4	Nov 2009	13.5	2.5	(1,3)	B
2.48 ± 0.15	Feb 2010	11.6	4.6	(1,3)	C
16.05 ± 0.11	Apr 2010	12.8	3.9	(1,3)	D
5.5	May 2010	15.2	1.0	(4)	E
24.40 ± 0.4	May 2010	14.7	1.2	(1)	F
27.8	Sep 2021	11.5	4.5	(5)	G
23.75	Oct 2021	13.1	2.5	(5)	H
3.41	Nov 2021	15.2	0.6	(5)	I

Notes. References: (1) Miles (2016); (2) this work; (3) Trigo-Rodríguez et al. (2010); (4) from Spanish amateur data (Kidger homepage); (5) R. Miles/J.-F Soulier.

3. Gas production rates

3.1. Modeling

To compute gas production rates, we modeled the excitation processes and radiative transfer in the coma following previous works (Biver 1997; Biver et al. 1999; Zakharov et al. 2007). Processes include collisions, excitation of the vibrational bands by the solar radiation, radiation trapping, and spontaneous decay. The excitation model computes the evolution of the populations of the rotational levels as the molecules expand radially in the coma.

Only collisions with CO molecules were considered because CO is the dominant molecule in the coma of 29P. Indeed, CO_2, found to be relatively abundant in many comets, has an abundance relative to CO lower than 1% in 29P (Ootsubo et al. 2012). As derived from this work (Tables 2, 6), water is also a minor constituent of the atmosphere of this distant comet. We assumed collisional cross-sections $\sigma_c(CO–CO) = 2 \times 10^{-14}$ cm^2, $\sigma_c(H_2O–CO) = 5 \times 10^{-14}$ cm^2, $\sigma_c(NH_3–CO) = 2 \times 10^{-14}$ cm^2, and $\sigma_c(HCN–CO) = 10^{-14}$ cm^2 (Biver et al. 1999). Collision rates were computed taking the relative masses of the colliding molecules into account. An important parameter for modeling collisional excitation is the gas temperature, which we assumed to be 6 K. This value is a compromise between the upper limit of 8 K derived from the line width of the blueshifted component of the $J(2–1)$ line (see Fig. 3), the value of 4 K estimated from CO $J(2–1)$ maps (Gunnarsson et al. 2008), and the CO rotational temperature of 4.9 $\pm$ 1.2 K, determined from infrared spectroscopy (Paganini et al. 2013). This low gas temperature is consistent with values expected at a few hundred kilometers from the nucleus of 29P on the basis of gas-dynamics

calculations (Crifo et al. 1999). For molecules released by the nucleus, the level populations evolve from local thermal equilibrium (LTE) in the collisional region to fluorescence equilibrium in the outer coma. The size of the LTE region is a function of the molecule. Molecules close to the nucleus, where the gas is warmer, do not contribute significantly to the measured signals because the large FOVs exceed 10^4 km in radius.

As discussed in Sect. 5, the characteristics of the H_2O and HCN lines suggest that these molecules are predominantly produced from icy grains at cometocentric distances $L_p > 10^4$ km where collisions with CO molecules are rare. Therefore, we also investigated the evolution of the level populations of H_2O and HCN molecules released at $L_p = 10^4$ and 5×10^4 km. We assumed that their initial rotational temperature is equal to 100 K, which corresponds to the expected equilibrium temperature of grains with radii > 20 μm (Sect. 5). Calculations were also made with an initial rotational temperature of 170 K to investigate the release from 2-μm organic grains. For this icy-grain production model, the molecules expand radially (a simplification that admittedly is not physically realistic) from L_p to outward. This truncated density distribution was used to infer production rates in the icy-grain model cases (Table 2).

3.2. CO production rate

Table 4 displays production rates derived for CO. The calculations take the peculiar shape of the CO line into account that has already been discussed in several papers (e.g. Gunnarsson et al. 2002, 2008). This shape is interpreted and modeled here as due to the combination of a CO jet with a 45° half-opening angle, expanding toward the Sun at a velocity of 0.5 km s^{-1}, and a complementary outgassing out of the jet cone expanding at 0.3 km s^{-1}. The total production rates given in Table 4 assume that the production rate in the jet component is 60% of the total production. We also provide in Table 4 the production rate in the
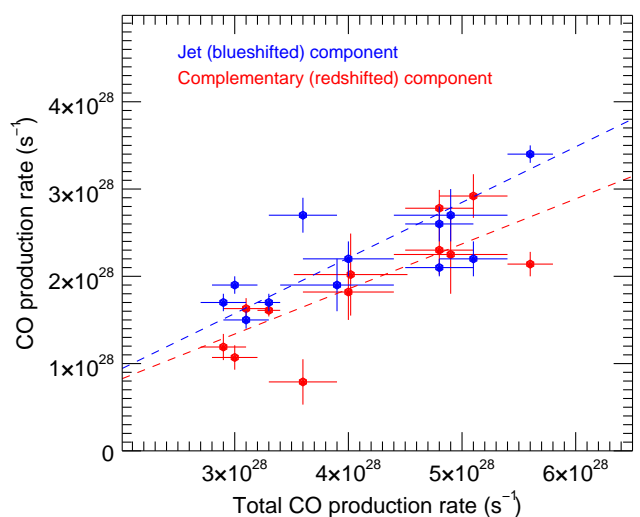
Fig. 5. CO production rates in the jet component (blue symbols) and complementary component (red symbols) as a function of the total CO production rate. They are inferred from the line areas measured between –0.7 and –0.3 km s^{-1}, and between –0.3 and +0.4 km s^{-1}, respectively. Values for the jet component and total production rates are given in Table 4. The dashed blue and red lines show linear fits to the data points that correspond to the jet and complementary components, respectively.

jet component, derived from the line areas measured between -0.7 and -0.3 km s^{-1} and using the same jet parameters as given above. The CO production rate in the jet component is between 43 and 75% of the total CO production rate, with a mean value of 54%, which is consistent with the previous assumption about the relative contribution in the two components. We do not observe any significant trend between the relative contributions of the two components and the total CO production rate (Fig. 5). The CO production rate on the various days is between 3 and 6×10^{28} s^{-1}, which is consistent with previous measurements (Senay & Jewitt 1994; Crovisier et al. 1995; Festou et al. 2001; Gunnarsson et al. 2002, 2008; Ootsubo et al. 2012; Paganini et al. 2013; Wierzchos & Womack 2020).
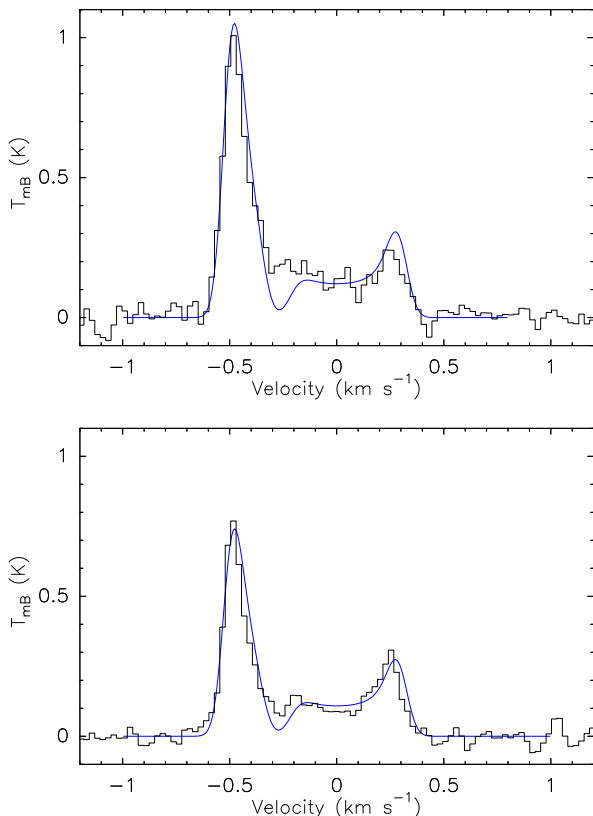

Fig. 6. Synthetic CO J(2-1) spectra (blue) superimposed on observed IRAM spectra (black). Top: Average data from 29 December 2007 to 11 January 2011 (mean r_h = 6.1 au and mean Δ = 5.5 au). The production rate in the sunward jet of $45°$ semi-aperture is 2.7×10^{28} s^{-1}, and the total CO production rate is 4.5×10^{28} s^{-1}. Bottom: Average November 2021 spectrum. The production rate in the sunward jet is 1.7×10^{28} s^{-1}, and the total production rate is 3.2×10^{28} s^{-1}. The outflow velocities within and outside the jet are assumed to be $v_{\exp}$ = 0.5 and 0.3 km s^{-1}, respectively.

Figure 6 shows synthetic CO spectra that reproduce to first approximation the average IRAM 2007–2011 and November 2021 spectra. A more realistic model providing a better fit would be the model used by Festou et al. (2001) (see also Gunnarsson et al. 2008), where the outgassing rate and expansion velocity both vary continuously with solar zenith angle.

3.3. H_2O production rate

In contrast to the CO line, the HCN and H_2O lines have approximately symmetric shapes (Sects 2.1 & 2.4). Therefore, we as-

sumed isotropic outgassing and adopted a velocity of 0.3 km s^{-1}, consistent with the half-width of these lines (0.23 ± 0.04, and 0.4 ± 0.2 km s^{-1} for H_2O and HCN, respectively, Sect. 2.1 and 2.4). The same assumptions were made to derive the upper limits on the NH$_3$ production rate.

A low level of water production is measured, with a mean value of $Q(H_2O) = (4.1 \pm 0.6) \times 10^{27}$ s^{-1} for April–May 2010, for the nucleus model which assumes water release from the nucleus (Table 2). Using CO production rates measured during this period, we derive a $Q(H_2O)/Q(CO)$ ratio of 10.0 ± 1.5 %. A 3σ upper limit $Q(H_2O)/Q(CO) < 8\%$ is measured for the period 30 December 2010 to 11 January 2011.

Both H_2O and CO were detected on 19 November 2009 (r_h = 6.18 au) with the *Akari* telescope, through their vibrational bands at 2.7 and 4.3 μm, respectively (Ootsubo et al. 2012). The water production rate derived from these measurements is ($6.3 \pm 0.5) \times 10^{27}$ s^{-1} (i.e. 1.5 times higher than the *Herschel* value) for a CO production rate of $(2.9 \pm 0.2) \times 10^{28}$ s^{-1}. Therefore, the $Q(H_2O)/Q(CO)$ ratio derived from the *Akari* data is 22 ± 2%. However, Ootsubo et al. (2012) assumed CO and water outflow velocities of 0.31 km s^{-1}. Using our velocity assumptions instead, we derive $Q(H_2O) = (5.9 \pm 0.5) \times 10^{27}$ s^{-1}, $Q(CO) = (3.8 \pm 0.3) \times 10^{28}$ s^{-1}, and $Q(H_2O)/Q(CO) = 15 \pm 2$ %, which is marginally higher than the *Herschel* value. We note that the FOVs for the two data sets are similar.

The water production rates derived for the icy-grain model with the nominal grain temperature assumption of 100 K are almost identical to those of the nucleus production model for L_p = 5×10^4 km. They are about three times lower for $L_p = 10^4$ km (Table 2). For $L_p = 10^4$ km, the average population within the HIFI field of view ($\sim 8 \times 10^4$ km radius) of the H_2O 1_{10} rotational level is indeed higher for the icy-grain model than for the nucleus-production model. For a grain temperature of 170 K, the derived production rates are 5% lower.

3.4. HCN production rate

The derived HCN production rate determined for the 2007–2011 period is 4.4×10^{25} s^{-1} when we assume direct release from the nucleus (Table 2). The value is almost the same (within 20–50%) when production from icy grains is considered.

The HCN production rate typically is a factor of 100 and 1000 lower than the H_2O and CO production rates, respectively. Using the April-May 2010 data alone and considering the nucleus-production model, we find $Q(HCN)/Q(CO) = (1.2 \pm 0.3) \times 10^{-3}$, and $Q(HCN)/Q(H_2O) = (1.2 \pm 0.3) \times 10^{-2}$. From the detection of CN in optical spectra of comet 29P obtained in December 1989, Cochran & Cochran (1991) measured a CN production rate $Q(CN) = 8 \times 10^{24}$ s^{-1}. This is a factor of 5 lower on average than the HCN production rate. This discrepancy might be related to the extended nature of the HCN production, as discussed in Sect. 5, or to comet variability.

The HCN abundance relative to water is a factor of 10 higher than values found in comets at 1 au from the Sun, which are typically $0.1–0.2 \times 10^{-2}$ (Bockelée-Morvan et al. 2004). However, compared with C/1995 O1 (Hale-Bopp) at 6 au (Biver et al. 2002) (we extrapolated the water production rate measured outbound at 5 au from the Sun to 6 au and used the $Q(HCN)$ measured at 6 au outbound), the $Q(HCN)/Q(H_2O)$ and $Q(HCN)/Q(CO)$ ratios in 29P are consistent within a factor of about three with the values measured in Hale-Bopp at 6 au post-perihelion (Table 6).

Table 6. Abundances relative to CO.

Quantity	29P $r_h \sim 6$ au	Comets $r_h \sim 1$ au	Hale-Bopp[a] $r_h \sim 6$ au
$Q(H_2O)/Q(CO)$	0.10	5–200[a,b,c]	≤ 0.08[g]
$Q(HCN)/Q(CO)$	0.001	0.01–0.5[a,b,c]	0.003
$Q(NH_3)/Q(CO)$	< 0.1	0.03–1.0[b,c,d]	–
$Q(CO_2)/Q(CO)$	< 0.01[e]	0.5–5[f]	–

Notes. Abundances derived assuming molecule release from the nucleus, a condition that is not verified at $r_h = 6$ au from the Sun. [a] Biver et al. (2002). [b] Dello Russo et al. (2016). [c]Lippi et al. (2021), excluding values from the hyperactive comet 103P/Hartley 2. [d] DiSanti et al. (2017). [e] Ootsubo et al. (2012). [f] A'Hearn et al. (2012), excluding the atypical value of 100 measured in 103P/Hartley 2.[g] Extrapolating the $Q(H_2O)$ trend observed post-perihelion.

3.5. NH$_3$ production rate

For NH$_3$, the derived 3σ upper limit for the average of April and May 2010 data is 4.5×10^{27} s^{-1} (nucleus-production model, Table 2). This upper limit is a factor of two lower than the previous best limit from Paganini et al. (2013). The abundance of NH$_3$ relative to water (< 1.1) is not constraining compared to values measured in comets near 1 au from the Sun (0.005, e.g. Biver et al. 2012).

Table 6 summarizes the molecular abundances relative to CO measured in 29P and Hale-Bopp at 6 au from the Sun, and in other comets. This table illustrates the strong differences in coma composition between distant comets and comets at $r_h \sim 1$ au.

4. Correlation between gas production and dust outbursts

Several HIFI and IRAM observations were obtained soon after outbursts (Sect. 2.5). Therefore, it is possible to investigate whether outgassing is correlated to the dust activity for either the quiescent or the outbursting stages.

4.1. Correlation of CO to dust

Figure 7 shows the time evolution of the CO production rate and R nuclear magnitude m_R in December 2007 and April-May 2010. The CO production rate is higher for higher coma brightness. The decay of the coma brightness after outburst D coincides with a decrease in CO production.

Figure 8 plots the CO production rates as a function of the elapsed time $\Delta T_{outburst}$ (Table 7) between outburst times and observing date, considering only IRAM data. The highest CO production rates are observed for $\Delta T_{outburst} \leq 10$ days and are all about 5×10^{28} mol s^{-1}. The figure might suggest that in some instances, $Q(CO)$ remains higher than the quiescent value up to 15–25 days (and even 40 days) after the most recent outbursts. However, the data points showing CO excess in this time range pertain to the observations of May 2010 with three consecutive outbursts (D, E, and F; bottom panel of Fig. 7).

To quantify the significance of the correlation, we enlarged the sample, especially for measurements during quiescent activity, by considering the CO $J(2–1)$ data acquired with the Arizona Radio Observatory 10 m Submillimeter Telescope (SMT) during the periods February-May 2016 and November 2018 to January 2019 (Wierzchos & Womack 2020). For consistency, the
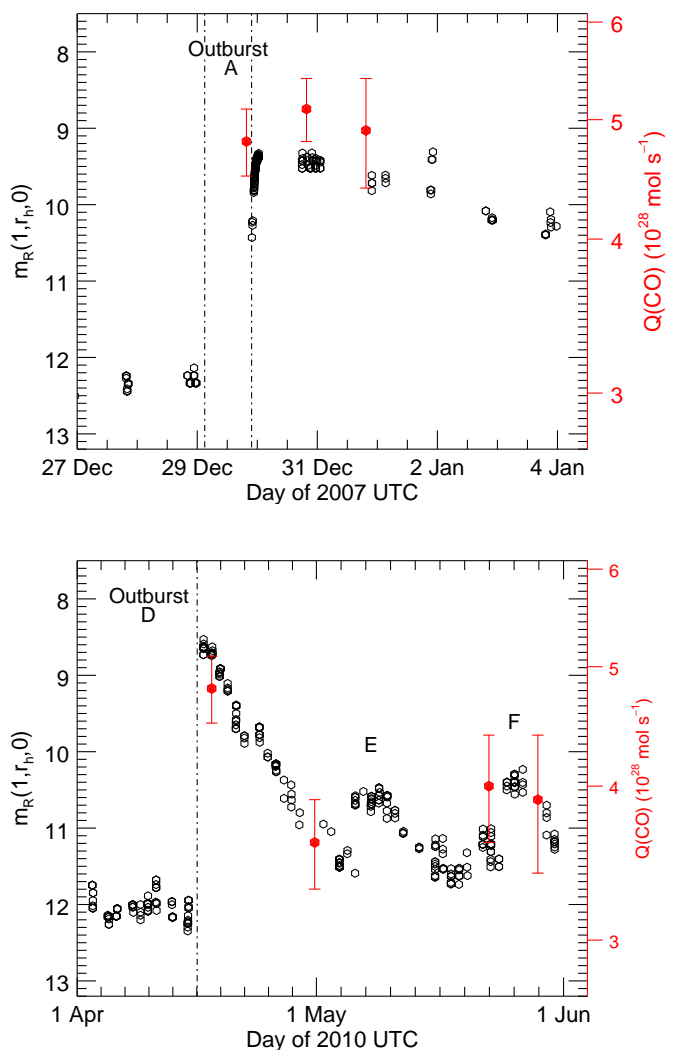
Fig. 7. CO production rates and reduced nuclear magnitudes in December 2007 and April-May 2010. The times of outbursts A and D are marked by dot-dashed lines. Outbursts E and F are also shown. The R nuclear magnitudes are measured inside an aperture with a diameter of 10″ (Spanish amateur data reported in Tables D.1 and D.2; homepage of M. Kidger). The relation between the CO and magnitude scales is $\log_{10}(Q(CO)) = 29.25 - 0.062 m_R(1, r_h, 0)$, consistent with Eq. 2.

CO production rates were recomputed using the published line areas, assuming a main-beam efficiency of 0.71, and using the same model and model parameters as were used to analyze the IRAM observations. The inferred CO production rates are very similar to those inferred by Wierzchos & Womack (2020).

Figure 9 shows the CO production rate as a a function of the the reduced magnitude $m_R(1, r_h, 0)$ defined in Sect. 2.5. IRAM and SMT data are merged. A linear fit between $\log_{10}(Q(CO))$ and $m_R(1, r_h, 0)$ gives

$$\log_{10}(Q(CO)) = (29.29 \pm 0.04) - (0.062 \pm 0.004) m_R(1, r_h, 0), \quad (2)$$

where the uncertainties do not consider magnitude errors. This fit is shown by a dashed line in Fig. 9. The Spearman rank correlation coefficient of $r_s = -0.67$ together with the small significance value of its deviation from zero ($p_{r_s} = 0.002\%$) and the number of standard deviations with respect to the null hypothesis ($z_D = 3.8$) are consistent with a moderate to strong correlation. The

(5)

Fig. 8. CO production rates as a function of the elapsed time $\Delta T_{outburst}$ between outburst time and observation date. The reference time for $\Delta T_{outburst}$ are outbursts A, C, D, and G (black dots), outbursts F and H (red dots), and outbursts E and I (blue dots). The color code is such that when several outbursts are relevant to a CO measurement, black color is for the brightest, blue colour for the faintest, and red color is for the 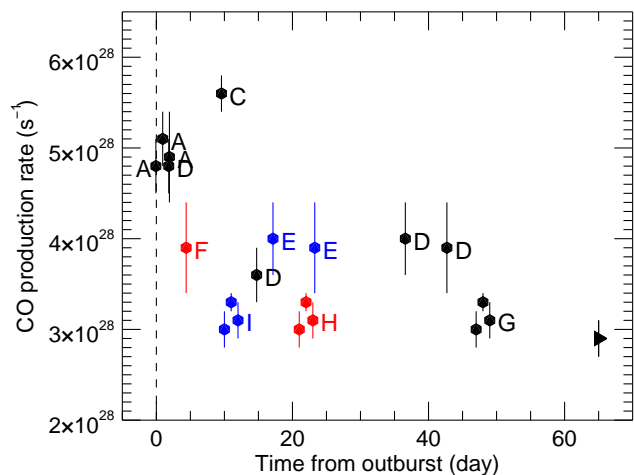outburst with intermediate brightness. The black triangle (rightmost data point) refers to the January 2011 measurement obtained more than 93 d after an outburst.

Spearman coefficient is $r_s = -0.87$ (with $p_{r_s} = 0.03\%$, $z_D = 2.9$) considering only IRAM data, and $r_s = -0.54$ (with $p_{r_s} = 1.1\%$, $z_D = 2.4$) for SMT data.

Several data points deviate significantly from the fit, and indeed Wierzchos & Womack (2020) found that two dust outbursts coincided with a rise in CO, but two other outbursts occurred without any substantial increase in CO production. At quiescent magnitudes, $Q(CO)$ is about 3×10^{28} s^{-1} (Fig. 9). We adopt in the following the central value of $Q_{quiet}(CO) = 2.9 \times 10^{28}$ s^{-1} determined by Wierzchos & Womack (2020) from 2016 CO data. The regression slope in the correlation equation (Eq.2) is small (0.062), and it is three times smaller than the value established for comet Hale-Bopp (0.22, Womack et al. 2021) (Appendix B). This is illustrated in Fig. 9 by the dot-dashed line.

Since at least two-thirds of the measured CO outgassing corresponds to permanent activity, we derived the correlation equation for the outburst material. The excess of CO production related to outbursts is given by

$$Q_{out}(CO) = Q(CO) - Q_{quiet}(CO). \tag{3}$$

The nuclear magnitude of outburst dust ejecta is calculated according to

$$
\begin{aligned}
m_{R,out}(1, r_h, 0) = &- 2.5\log_{10}(10^{-0.4m_R(1,r_h,0)} \\
&- 10^{-0.4m_{R,quiet}(1,r_h,0)} - 10^{-0.4m_{R,nuc}(1,r_h,0)}),
\end{aligned} \tag{4}
$$

where $m_{R,quiet}(1, r_h, 0)$ (= 13.4) is obtained from Eq. 2. $m_{R,nuc}(1, r_h, 0)$ is the nucleus magnitude (equal to 14.04 at $r_h = 6$ au), derived from an expected R absolute magnitude of 10.15, assuming a nucleus radius of 31 km and a R geometric albedo of 0.044.

Using IRAM and SMT data, we obtain

$$\log_{10}(Q_{out}(CO)) = (29.40 \pm 0.04) - (0.127 \pm 0.003)m_{R,out}(1, r_h, 0),$$

and the Spearman rank correlation coefficient is $r_s = -0.55$ (with $p_{r_s} = 0.2\%$, $z_D = 2.9$). Using the IRAM data alone, we obtain

$$\log_{10}(Q_{out}(CO)) = (29.98 \pm 0.05) - (0.172 \pm 0.004)m_{R,out}(1, r_h, 0), \tag{6}$$

with $r_s = -0.82$, $p_{r_s} = 0.2\%$, $z_D = 2.6$. Figure 10 shows $Q_{out}(CO)$ as a function of $m_{R,out}(1, r_h, 0)$, and the linear fits given by the correlation equations Eq. 5 and 6. The correlation law for 29P is very close to the $Q(CO)/m_R(1, r_h, 0)$ correlation established for comet Hale-Bopp at large heliocentric distances, where the activity was dominated by CO outgassing (Eq. B.2, dotted red line).
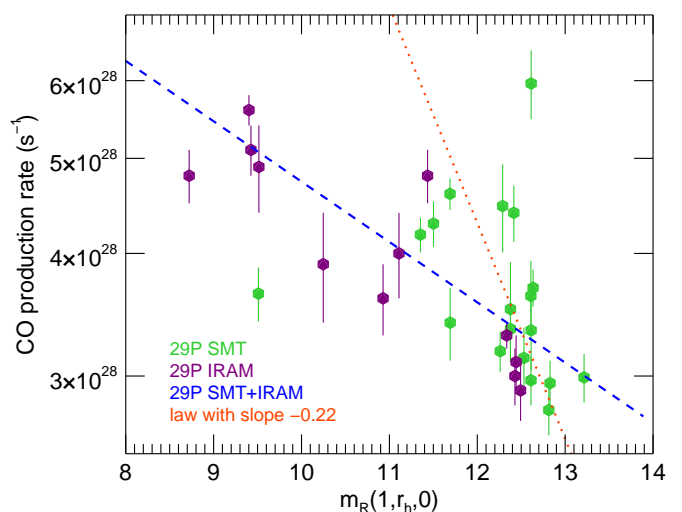
Fig. 9. CO production rates as a function of $\Delta-$ and phase–corrected red nuclear magnitude $m_R(1, r_h, 0)$. Purple symbols show CO data from this work. Green symbols show CO data from Wierzchos & Womack (2020). The dashed blue line shows the fit to all data (Eq. 2). The dotted red line shows the curve $\log_{10}(Q(CO)) = K - 0.22\, m_R(1, r_h, 0)$, whose regression slope corresponds to that measured for comet Hale-Bopp (K here is an arbitrary constant and not the constant appearing in the Hale-Bopp correlation equation Eq. B.4).

4.2. H_2O and HCN correlations with CO outgassing

The two HIFI water detections were obtained 3 and 25 days after the major outburst D (Sect. 2.5). The signal decreased by a factor 1.45± 0.42 between the two dates. The same decrease (by a factor 1.41±0.15) is observed for the CO line area; this is shown by a comparison of the values at 1.8 and 15 d after outburst D. At the date of the H_2O nondetection (30 December 2010), 29P was quiescent (and the CO production rate measured 12 days later was at the quiescent value). These trends, together with the similarity between *Akari* and *Herschel* $Q(H_2O)/Q(CO)$ measurements, suggest a correlation between water and CO production. On the other hand, there is no apparent correlation between the HCN and CO line areas, but the low signal-to-noise ratio of the HCN line area prevents any definitive conclusion.

Taking into account that at least two-thirds of the measured CO outgassing is not related to recent outbursts, but corresponds
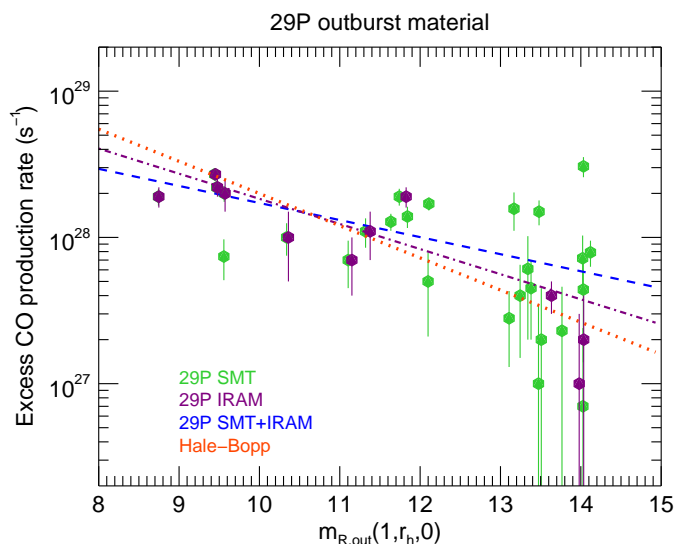
Fig. 10. Same as Fig. 9, but considering the contribution of outburst material. The dashed blue line shows the fit to all 29P data (Eq. 5). The dot-dashed purple line shows the fit to IRAM 29P data (Eq. 6). The dotted red line shows the curve $\log_{10}(Q(CO)) = 30.5 - 0.22\, m_R(1,r_h,0)$ determined for comet Hale-Bopp (Appendix B).

to permanent activity, the constant H_2O/CO production rate ratio suggests that H_2O is present in the atmosphere of comet 29P even during quiescent phases. The H_2O/CO correlation (if confirmed) is surprising. As discussed in the next section, H_2O and HCN are released in the outer coma by long-lived icy grains, whereas CO molecules are outgassing from the near-nucleus region. This correlation could be explained if the dust-to-gas production rate ratio during outburst and quiescent phases were similar, but this contradicts the measurements (see the next section).

4.3. Constraints on the origin of outbursts

A well-documented outburst is the huge (m_R from 16.5 to 6.5) outburst of comet 17P/Holmes on 24 October 2007. A high CO production rate of 1.8×10^{29} mol s^{-1} was observed at the IRAM 30 m telescope two days after the onset of the outburst, followed by a steep decrease by a factor of 6.3 between $\Delta T_{\text{outburst}} = 2$ d and $\Delta T_{\text{outburst}} = 7.5$ d (Biver et al. 2008). This is consistent with the rapid vaporization of icy debris and the short residence time of the CO molecules within the IRAM beam (typically 0.07 d for 17P at $\Delta \sim 1.62$ au). In this time interval, m_R varied from 6.5 to 8.4. For 29P, the residence time of the CO molecules is 0.7 d, and the residence time is 1.7 d for the dust particles outflowing at 0.15 km s^{-1} (Sect. 2.5). The constancy of $Q(CO)$ within 2–3 days after the December 2007 outburst (Fig. 7) suggests continuous CO production either from the outburst ejecta or from the nucleus surface areas from which the outburst was triggered. The amount of CO that was released during outbursts A and D can be roughly estimated by assuming that most of the production occurred within 5 days after outburst onset at a rate of 2×10^{28} mol s^{-1}. The derived CO mass is $\sim 4 \times 10^8$ kg, which corresponds to a 47 m radius sphere of pure CO ice. The few available estimates of the mass of dust in outburst ejectas give lower limits of 3–18×10^8 kg (Hosek et al. 2013; Schambeau et al. 2017). Assuming that CO is intimately mixed with nucleus material (with

density $\rho_N = 500$ kg m^{-3}), the nucleus volume affected by CO vaporization is $0.64\ 10^{-6}$ % of the total volume of the nucleus.

The outbursts of 29P are observed with some periodicity (7.3 per year), which caused Trigo-Rodríguez et al. (2010) to conclude that the triggering mechanism involves a periodic insolation of a particular region associated with the nucleus rotation with a presumed period ~ 57 d. Miles (2016) refined the analysis and suggested at least 6 discrete outburst sources that are grouped in longitude (within 15°) on the surface of the nucleus. The similarity of the CO line profiles during outburst and quiescent phases (Figs 3 and 5) confirms that outbursts occur in the subsolar region, where CO outgassing predominantly and continuously operates.

The established correlation laws between CO production rates and magnitudes, both in quiescent and outburst state, and the comparison with comet Hale-Bopp provide insights into the properties of outbursting regions. We first mention that the size of comet Hale-Bopp (37 ± 3 km, Szabó et al. 2012) is similar to that of 29P, so that processes involving gravity, such as the dynamics of large particles, and their gravitational fallback, might be comparable.

The CO production rate of 29P during quiescent activity is very similar to that of comet Hale-Bopp at 6 au from the Sun ($\sim 3 \times 10^{28}$ s^{-1} inbound and $\sim 2 \times 10^{28}$ s^{-1} outbound, Biver et al. 2002). On the other hand, with $m_{R,\text{quiet}}(1, r_h, 0) = 13.4$ for 29P and $m_R(1,r_h,0) \sim 9$ at $r_h = 6$ au for Hale-Bopp (Appendix B), the quiescent dust activity of the two comets is different by more than one order of magnitude in brightness. This can be explained by two scenarios. The first scenario is differences in surface properties: A higher cohesion of the surface material of 29P could quench dust activity, or large particles on the surface (e.g. fallback particles) might reduce dust-gas coupling and thus dust lifting; see the discussion in Tubiana et al. (2019). The second scenario is differences in size properties of the lifted dust particles. A deficiency in small particles in the quiescent coma of 29P (i.e., a minimum particle size larger than in the coma of Hale-Bopp) would result in a lower coma brightness in the optical for the same dust production rate in kg/s; this would also imply different surface properties in terms of particle size distribution. The dust production rate of comet Hale-Bopp at large heliocentric distances is well constrained by mid-IR data (Grün et al. 2001) and detailed modeling of optical data (Weiler et al. 2003). At 6 au outbound, the value determined by Weiler et al. (2003) is approximately 10^3 kg s^{-1}, about a factor of ten higher than the quiescent value for 29P (Sect. 6.4). Therefore, this favors the first scenario, in which the dust activity of 29P (but not the gas activity) is quenched, possibly as a result of surface-subsurface processing induced by activity.

In contrast, the outburst activity of 29P presents similarities with the continuous activity of Hale-Bopp. The fact that the $Q(CO)$ and visual magnitude correlations for the outburst material of 29P and for Hale-Bopp are very similar (Fig. 10) indicates a similar dust-to-gas flux ratio for the outburst ejecta of 29P and the continuous activity of Hale-Bopp (we refer here to dust particles that contribute to the scattering cross-section). Overall, this suggests strong local heterogeneities on the surface of 29P, with quenched dust activity from most of the surface, but not in outbursting regions.

Several triggering mechanisms for the 29P outbursts have been proposed, but the driving process remains unknown. The proposed scenarios include 1) the amorphous-to-crystalline phase transition of water, and 2) the build-up of high-pressure pockets of hypervolatiles below the surface layers. On comet 67P, the spatial distribution of outburst locations on the nu-

cleus correlates well with areas marked by steep scarps or cliffs (Vincent et al. 2016), and 45% of the 67P summer outbursts occurred near local noon. Some events were found to be initiated by the collapse of a cliff (Pajola et al. 2017; Agarwal et al. 2017), and thus to be simply related to erosion (scenario 3). As discussed by Vincent et al. (2016), activity from fractured cliffs leads to a weakening of the wall structure until it collapses. Cliffs should be more instable on larger bodies such as 29P. For these three scenarios, we expect an increase of CO outgassing correlated with dust release. The measured CO release shows that large areas on the 29P surface are affected during outbursts. We hypothesize that the slow (57 d) rotation of 29P plays a role for the driving mechanism, as it allows the heat wave to penetrate deeper into the subsurface layers. We propose a fourth scenario, namely that outbursts result from fractures (or pits) on the 29P surface. From thermophysical modeling, Höfner et al. (2017) showed that, through the effect of self-heating, fractures are an efficient heat trap when the Sun shines directly into the fracture, resulting in enhanced outgassing with respect to a flat surface during illumination. This scenario could explain both the periodicity of the outbursts, and the higher dust-to-gas flux ratio observed during outbursts, if fracture floors are structurally less evolved than the remaining surface. For a 10-min-long outburst, the typical size of the illuminated fracture floor would be 25 m, but this would be 3 km for a one-day-long outburst.

5. Water production and origin of H_2O and HCN

5.1. Evidence for production by sublimating icy grains

The observed water production rate might be explained by outgassing from the nucleus surface. The thermal properties of the nucleus of 29P have been constrained by multiwavelength *Spitzer* observations (Stansberry et al. 2004; Schambeau et al. 2015, 2021). Using the Near Earth Asteroid Thermal Model (NEATM, Harris 1998), Schambeau et al. (2021) inferred an infrared beaming factor $\eta=1.1\pm0.2$, consistent with the mean value of 1.03 ± 0.11 determined for an ensemble of 57 Jupiter-family comets (Fernández et al. 2013). When we adopt $\eta = 1.03$, a gray emissivity of 0.95 and a Bond albedo of 0.012, the temperature of the subsolar point is equal to 158.59 K at $r_h = 6.21$ au. At this temperature, a sublimating area of ~2000 km^2 of crystalline ice is needed to supply a rate of 4.1×10^{27} s^{-1} of water molecules. However, with a rotation period of ~57 days (based on the periodicity of the outbursts, Miles 2016), and an expected small thermal inertia, as measured for other Centaurs and cometary nuclei (Groussin et al. 2013; Fornasier et al. 2013; Lellouch et al. 2013; Gulkis et al. 2015), we expect variations in the surface temperature with solar zenith angle, and low temperatures on the night side. In order to compute the active fractional area of the nucleus surface that supplies the observed water production rate, we therefore applied the sublimation model of Cowan & A'Hearn (1979), which computes the latitude dependence of the surface temperature and sublimation rate. We used the model outputs for a rotational pole pointed at the Sun, which is identical to both the nonrotating case and to the case of zero thermal inertia. It is therefore appropriate for investigating the activity of 29P. The derived active fractional area is 440%, suggesting that sublimating icy grains contribute mainly to water vapor release in the atmosphere of 29P. This active fractional area is in the upper range of values measured for hyperactive comets (Lis et al. 2019). The vapor pressure of amorphous ice is one to two orders of magnitude higher than for crystalline ice (see Fray & Schmitt 2009, and references therein), which means

that the fractional area of amorphous ice would be lower. However, we do not expect water ice to be in amorphous form in the near-surface layers of the nucleus of 29P (Enzian et al. 1997; Kossacki & Szutowicz 2013).

The low velocity offset observed for the H_2O line ($\Delta v= -0.08\pm0.05$ km s^{-1}, Table 2) also suggests that the nucleus contributes little to the water production. Water sublimation is indeed expected to be most efficient near the subsolar point. Because of the low phase angle ($\phi < 10°$), such localized outgassing would have resulted in a line shape that is blueshifted by a fraction of kilometers per second, as observed for CO (Δv between –0.3 and –0.2 km s^{-1}).

HCN has a higher vapor pressure than water. We calculated that the observed production rate would correspond to an area of sublimating HCN ice of 4×10^{-3} km^2, assuming that this area is at the subsolar point. In this respect, the nucleus itself might therefore contribute to HCN production. However, the HCN line also presents a small velocity offset ($\Delta v= -0.04\pm0.07$ km s^{-1}; Table 2), so that its production is likely associated with that of water.

It is thus very likely that both HCN and H_2O are the products of icy-grain sublimation. Direct and indirect evidence for the presence of icy grains in cometary atmospheres is now numerous (e.g. Davies et al. 1997; Lellouch et al. 1998; A'Hearn et al. 2011; Fougere et al. 2012; Protopapa et al. 2014). In particular, the spectroscopic signature of water-ice grains has been detected in comets at large r_h as in C/1995 O1 (Hale-Bopp) (7 and 2.9 au, Davies et al. 1997; Lellouch et al. 1998), C/2002 T7 (LINEAR) (3.5 au, Kawakita et al. 2004), and C/2013 US_{10} (Catalina) (3.9 to 5.8 au, Protopapa et al. 2018).

5.2. Size constraints for sublimating icy grains

We computed (Appendix C) the temperature, velocity, and H_2O sublimation lifetime of icy grains as a function of size, for several grain compositions (olivine or amorphous carbon, referred as dirt or impurities) and ice contents. The results are shown in Fig. 11, panels a–c. Velocities were computed for the initial mass (before water release) of the grains. The sublimation lifetime is defined as the time when ice is exhausted. Calculations were made for volume fractions of dirt, v_i (i for impurities), of 0.1 and 0.5, corresponding to ice mass fractions of 78% and 29%, respectively (Appendix C.2). Figure 11d plots the scale length of the sublimation of icy grains, defined as the product of the grain-sublimation lifetime and the velocity of the grains (i.e. it is assumed that the motion of the grains is radial). As shown by Gunnarsson (2003), grains exhaust most of their ice content at a time similar to their lifetime. Figure 11a shows that, except for ice-rich olivine mixtures ($v_i = 0.1$), grains with sizes smaller than 1 μm reach temperatures higher than 160 K, so that they lose their ice content very quickly (in less than 1000 s). As expected, carbon grains reach higher temperatures than olivine grains, and grains with a higher content of dirt are generally warmer. The computed velocity of grains with a radius of 10 μm is 85 m s^{-1} considering CO anisotropic outgassing, and 35 m s^{-1} in the isotropic case (Fig. 11b). These values are similar to the few measured values. For 29P in quiescent state, one estimate is 35 m s^{-1} for particles with $\beta = 400$ (ratio of solar radiation pressure and solar gravity forces), corresponding to $a = 10$ μm for $\rho_d = 500$ kg m^{-3} (Fulle 1992). Measurements after an outburst lead to 150 ± 50 m s^{-1} (Feldman et al. 1996, , see also Sect. 2.5) to 250 ± 80 m s^{-1} (Trigo-Rodríguez et al. 2010) for typically 1 μm sized particles which extrapolate to 25–110 m s^{-1} for 10 μm grains.
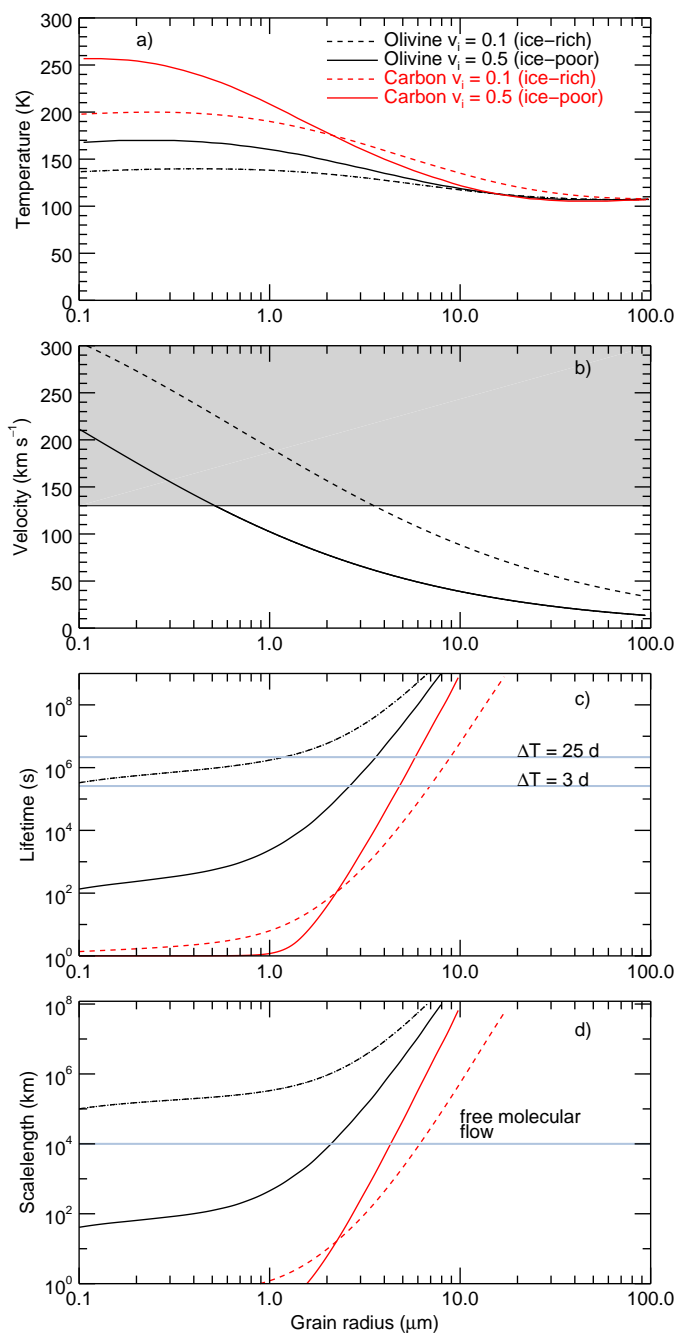
Fig. 11. Properties of icy grains as a function of size. a) Grain temperature. b) Grain velocity computed assuming a CO production rate of 4 × 10²⁸ s⁻¹ emitted in a cone with a half-angle equal to $\psi = 45°$ (dashed curve) or $\psi = 180°$ (solid curve), and a dust and nucleus density equal to 500 kg m⁻³. Velocities in the gray region are excluded at 1σ from the velocity offset of the H_2O and HCN lines. c) Grain-sublimation lifetime; the two horizontal blue dotted lines correspond to the elapsed time between the 16.05 April 2010 outburst and the *Herschel* H_2O observations. d) Scale length defined as the product of the grain-sublimation lifetime times the grain velocity (calculated with $\psi = 45°$); the horizontal line corresponds to the limit of CO free-molecular flow (see text). In panels a), c) and d) the black and red curves correspond to crystalline ice mixed with olivine and carbon, respectively. Solid and dashed lines show ice-poor grains ($v_i = 0.5$, ice mass fraction of 29%) and ice-rich grains ($v_i = 0.1$, ice mass fraction of 78%), respectively.

The low velocity offset of the H_2O and HCN lines provides some constraints on the size of the icy particles. A significant

contribution from small (radius $a < 3\ \mu m$ according to Fig. 11b) grains to the observed HCN and H_2O molecules is excluded at the 1σ level, because their significant velocity would have resulted in a significant negative velocity offset in the spectra. At the 3σ level, the limiting minimal size is $\sim 1\ \mu m$. We assumed here that the grains originate from the sunlit hemisphere and are entrained by the CO jet (i.e., we consider the dashed curve in Fig. 11b).

The shapes of the HCN and H_2O lines are symmetric within the noise, unlike the strongly asymmetric line of the main coma constituent CO. This also indicates that these molecules are produced in a region in which collisions with CO molecules are rare. In the collisional region, extensive momentum exchange causes a coupling between its components, so that the distribution and kinetics of minor species follow those of the main constituent (e.g. Tenishev et al. 2008). Crifo et al. (1999) showed that the collisional region in comet 29P is much larger than 700 km. In their highly anisotropic case, the Knudsen number K_n (the ratio of the molecular mean free path length to a representative physical length scale) is equal to a few 10^{-2} at 500 km from the nucleus, which sets the inner boundary for the almost free molecular flow to typically $\sim 10^4$ km. Comparing this value to the grain-sublimation scale length as a function of size (Fig. 11d), we can exclude a major water-outgassing contribution from short-lived olivine-rich grains ($v_i = 0.5$) with $a < 2\ \mu m$. For carbon-rich grains, excluded grains are those with $a < 6.1\ \mu m$ ($v_i = 0.1$, ice rich) and $a < 4.3\ \mu m$ ($v_i = 0.5$, ice poor). However, the sub-μm olivine-rich grains with a high ice content ($v_i = 0.1$) sublimate outside the collision zone. HCN is more volatile than H_2O and should be exhausted more rapidly than water if it is present as pure HCN ice in grains. The symmetric HCN line shape suggests that HCN production occurs in the collisionless region and is controlled by the sublimation of water ice.

The H_2O and HCN line widths provide further constraints on the properties of the grains. Assuming isotropic ejection from the grains in a collisionless environment, the half-line width corresponds to the terminal velocity for free-molecular expansion, which is equal to the mean thermal speed: $v_{therm} = \sqrt{8k_B T_d/\pi m_{H_2O}}$ for water, where T_d is the grain temperature and m_{H_2O} is the mass of one water molecule. The range of inferred T_d is 36–64 K using the measured H_2O line width and its 1σ uncertainty (and $T_d > 62$ K using the HCN line width). This is indicative of low-temperature grains. However, the inferred T_d is a factor of two lower than the equilibrium temperature expected for large ($> 10\ \mu m$) grains (Fig. 11a). The low signal-to-noise ratio on the H_2O line is a possible explanation.

In conclusion, the characteristics of the HCN and H_2O line profiles suggest their production from long-lived icy grains with a size exceeding a few micrometers. We present in the next section results obtained from the strength of the water line.

5.3. Sublimating icy grains: outburst contribution and production rate

We modeled the production of water molecules by icy grains in the coma during an outburst (Appendices C.3–C.4) with the aim to study the evolution of the H_2O signal in the HIFI beam from 19 April to 11 May 2010 after outburst D.

The outburst is described by a boxcar function defined by its duration and dust production rate Q_{dust}. The number density of the H_2O molecules as a function of distance to nucleus was computed at a time interval with respect to outburst onset $\Delta T_{outburst} = 3$ d and 25 d, for comparison with HIFI water obser-

vations (Tables 1, 2). Grain sublimation was modeled following Appendix C.3, considering the carbon/ice-rich and ice-poor mixtures presented in Sect. 5.2. Grains composed of olivine are too cold to produce significant amounts of water vapor (Fig. 11a). The particle size distribution follows a power law $n(a) \propto a^\alpha$, where α is the size index, and the particle radius takes values from a_{min} to a_{max}. We ran the model with various sets of parameters for the size distribution and the outburst duration. A small subset of the model results is given in Fig. 12, where the outburst duration is set to two days.

At $\Delta T_{outburst}$ = 3 d from onset, all the molecules released by the outburst are at distances less than the radius of the FOV ($\sim 8.0 \times 10^4$ km). Therefore Q_{dust} can be readily estimated from the radial density profiles corresponding to $\Delta T_{outburst}$ = 3 d (leftmost curves in Fig. 12) to reproduce the number of molecules detected in the HIFI beam on 19.05 April 2010 (estimated as $\sim 10^{33}$ molecules from the nucleus production model, Sect. 3.3). In Fig. 12 results are shown for a_{max} = 50 μm, α = −3.5, carbon ice-poor and ice-rich mixtures, and two values of a_{min}. The inferred Q_{dust} are given in the plot. For a_{min} = 3 μm, the derived dust production rate is 1.1×10^3 kg/s (ice rich) to 4.3 10^3 kg/s (ice poor), that is, m_{dust} of $(2.0–7.4) \times 10^8$ kg released within two days. It reaches 6.6×10^4 kg/s (ice rich) to 1.7×10^7 kg/s (ice poor) for a_{min} = 8 μm (i.e., m_{dust} of 1.1×10^{10} and 2.9×10^{12} kg, respectively, released within two days). The inferred Q_{dust} increases with increasing a_{min} since the grain temperature decreases with increasing size. Q_{dust} also increases for shallower size distributions: For example, for α = −3.0, a_{min} = 3 μm, a_{max} = 50 μm, Q_{dust} is enhanced by a factor of two with respect to the case α = −3.5. The assumed maximum size a_{max} also affects the results: For a_{min} = 3 μm, and α = −3.5, Q_{dust} increases by a factor of 2.6 when a_{max} is changed from 50 to 250 μm. This is an expected result as the largest particles contribute only weakly to water production. The value a_{max} = 250 μm corresponds to the maximum size that can be lifted from the nucleus of 29P (Sect. 6.4). In Sect. 5.2 we show that the shape of the H_2O line profile suggests $a_{min} > \sim 4\,\mu$m and $a_{min} > \sim 6\,\mu$m when we assume ice-poor and ice-rich particles, respectively. Using these size constraints, we then derive a confident lower limit to the loss rate of icy particles during outburst D of $\sim 1.0 \times 10^4$ kg/s (ice poor) and $\sim 1.5 \times 10^3$ kg/s (ice rich).

The density profiles at $\Delta T_{outburst}$ = 3 d follow a Haser-type distribution for distances > 2×10^4 km (Fig. 12), but show a deficit in H_2O molecules at smaller distances. Molecules produced at small distances (essentially by small warm enough grains) moved to larger distances in the elapsed time since their production. The inner cutoff in the density profile is a function of the outburst duration and is no longer observed when the outburst duration is set to a value equal to 3 d (i.e. equal to $\Delta T_{outburst}$). The calculated Q_{dust} (and m_{dust}) does not vary much with the outburst duration when set to a value ≤ 3 d.

At $\Delta T_{outburst}$ = 25 d, the water shell is far away from nucleus center (> 10^5 km, rightmost curves in Fig. 12), and the total number of water molecules released by the icy grains increases. Only a fraction of them resides in the HIFI line of sight. Figure 13 shows the ratio of the calculated H_2O column density within the HIFI beam at $\Delta T_{outburst}$ = 25 d to the value at $\Delta T_{outburst}$ = 3 d (this ratio is referred to as ζ in the following). In this figure, a_{max} = 50 μm, α = −3.5, and a_{min} takes different values from 3 to 20 μm. The x-axis provides the Q_{dust} values reproducing the HIFI water measurement at $\Delta T_{outburst}$ = 3 d. The measured H_2O intensity ratio of ζ = 0.73 ± 0.21 is shown with a gray box for comparison. The calculated H_2O column density ratio ζ globally increases with increasing a_{min}. Figure 13 shows that the model output and

the measured evolution of the H_2O signal[8] match well for values of a_{min} higher than typically 5–7 μm, depending on the ice content. The Q_{dust} values consistent with the evolution of the H_2O signal are then > 2×10^4 kg/s (ice rich, $m_{dust} > 3.5 \times 10^9$ kg) and > 1×10^5 kg/s (ice poor, $m_{dust} > 2 \times 10^{10}$ kg). The limiting a_{min} values consistent with the evolution of the H_2O signal are slightly higher than those obtained from the H_2O line shape ($a_{min} > 4–6$ μm, Sect. 5.2).

Outburst D was followed by minor outburst E on 5.5 May 2010. In addition, the activity of 29P remained above the quiescent value in the time interval between outburst D and the 11 May observation (Fig. 7). Both outburst E and this continuous activity possibly contributed to the water molecules detected on 11 May 2010. Hence, the masses derived from the evolution of the H_2O signal might be overestimated.

In conclusion, the HIFI observations of water on 19 April 2010 suggest a Q_{dust} lower limit for outburst D ejecta of 1.5×10^3 kg/s (2.6×10^8 kg in two days). Compared with the excess of CO production (2×10^{28} s^{-1}) related to the outburst, the inferred lower limit for the dust-to-CO production rate ratio (in mass) is about 1.6. When we use the constraints obtained from the variation of the H_2O signal, we obtain $Q_{dust}/Q(CO) > 22$ (in mass). Icy grains released during outbursts might contribute significantly to the water molecules present in 29P coma, even long after an outburst. This might explain the high production rate measured by *Akari* nine days after an outburst of moderate amplitude (Sect. 3.3).
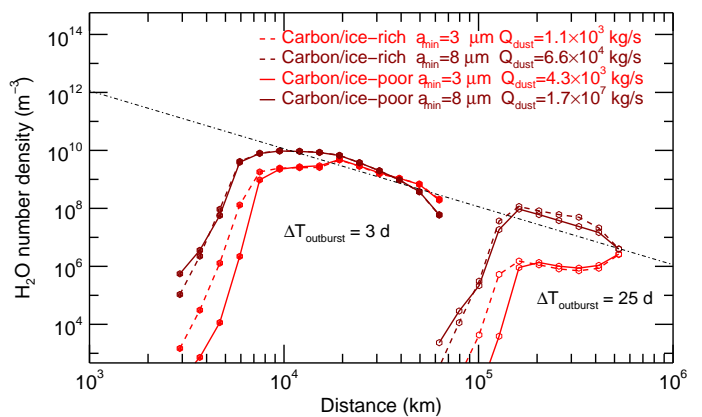
Fig. 12. Radial H_2O number density in the coma of 29P after an outburst releasing icy grains during two days at a rate Q_{dust}. The results are shown for an elapsed time $\Delta T_{outburst}$ = 3 d from the onset of the outburst (plain symbols, leftmost curves) and $\Delta T_{outburst}$ = 25 d (open symbols, rightmost curves). Q_{dust} (given in the legend) is set so that the number of molecules within the HIFI beam (whose projected radius is $\sim 8 \times 10^4$ km) is 10^{33} molecules at time $\Delta T_{outburst}$ = 3 d, corresponding to the 19.05 April 2010 measurement. The results for a_{min} = 3 and 8 μm are shown in red and dark red, respectively. The maximum grain radius is a_{max} = 50 μm, and the size index is α = −3.5. Results are shown for both ice-poor (v_i = 0.5) and ice-rich (v_i = 0.1) carbon grains. The dot-dashed line is a Haser model with $Q(H_2O) = 4.6 \times 10^{27}$ s^{-1} and expansion velocity v_{H_2O} = 0.25 km s^{-1}.

---

[8] Calculations considering the time evolution of H_2O excitation once released from grains (Sect. 3.1), that is that all molecules are not in the same excitation state, lead to similar conclusions.
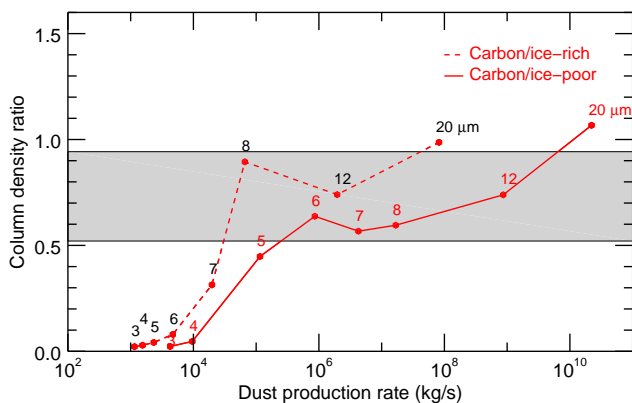
Fig. 13. Model outputs for the ratio of the H_2O column densities within the HIFI beam at $\Delta T_{outburst}$ = 25 d and $\Delta T_{outburst}$ = 3 d (referred as to ζ in the text). For comparison, the measured intensity ratio of 0.73 ± 0.21 between 11 May 2010 and 19 April 2010 is indicated by the gray region. For all models, the number of molecules within the HIFI beam is 10^{33} molecules at time $\Delta T_{outburst}$ = 3 d, corresponding to the 19.05 April 2010 observation, and the derived dust production is given in the x-axis. The model parameters are the outburst duration of 2 d, a_{max} = 50 μm, and α = −3.5. a_{min} takes different values from 3 to 20 μm, which are indicated (in μm units) on the plot above the corresponding model results. Results are shown for both ice-poor (v_i = 0.5) and ice-rich (v_i = 0.1) carbon grains.

6. Analysis of PACS data

We performed aperture photometry on the PACS 70 and 160 μm continuum images (Fig. 2) to provide estimates of the thermal flux detected from the nucleus and the dust coma. For the aperture photometry measurements, we applied two types of aperture corrections, depending on whether the flux within the aperture originated from the nucleus or the coma. The nucleus point-source contribution included aperture corrections based on the encircled energy fraction values presented in Table 7.4 of PACS handbook (version 4.0.1). For the coma, the aperture corrections were determined by comparing aperture photometry measurements of a synthetic $1/\rho$ coma profile (where ρ is the sky-plane projected cometocentric distance) versus a $1/\rho$ profile convolved with the PACS point spread function (PSF; Bocchio et al. (2016)). No color corrections were applied to the measurements. After inspection of Table 7.5 of the PACS handbook, we determined these corrections to be at the ∼ 1% level, well below the dominant uncertainty produced by the coma modeling and removal procedure.

6.1. Modeling and removing the coma

To obtain nucleus photometry measurements from the PACS images, the flux from the coma was modeled and removed. We used a well-established modeling technique (Lamy & Toth 1995; Lisse et al. 1999; Fernandez 1999) for this procedure, where the coma brightness distribution with azimuth and radial distance is measured in regions outside of significant contribution from the nucleus PSF in order to generate a synthetic coma model. The flux contribution of the modeled coma is then subtracted from the observations resulting in an approximately bare-nucleus residual image. The PSF models used in the analysis were from Bocchio et al. (2016).

The coma modeling and removal procedure was applied to each of the three 70 μm images from the three epochs of PACS

data (Table 1), resulting in three independent measurements of the spectral flux density of the nucleus that are reported in Table 7. Figure 14 provides an example of the results of the process. The quality of the coma removal and nucleus flux extraction process can be seen by the consistent noise pattern present in the residual image (right panel of Fig. 14). The 160 μm data do not have sufficient detections of extended coma surface brightness for the application of this technique. For the 160 μm data, we therefore applied a different technique to disentangle the detected nucleus versus coma flux, which is described below.

6.2. Nucleus thermal emission

We applied the NEATM model to each of the three epochs of 70 μm PACS images. Since extracted nucleus flux density measurements were only possible from the 70 μm data, our NEATM fits only included the effective radius of the nucleus as a free parameter. A value of η = 1.03 was assumed for the beaming factor based on the results of the Survey of Ensemble Physical Properties of Cometary Nuclei (SEPPCoN; Fernández et al. 2013). Additionally, we used similar assumptions as SEPPCoN for the bolometric Bond albedo A = 0.012 (assuming a visible-wavelength geometrical albedo p = 0.04 and phase integral relation q = 0.290 + 0.684G, Harris & Lagerros (2002)), emissivity ϵ = 0.95, and slope parameter G = 0.05. Using these assumptions, we derived three independent estimates of the effective radius of the nucleus that are reported in Table 7. These estimates (R_N between 30.3 and 31.9 km with 10% uncertainty) are within the uncertainties of the recent values for 29P reported in Bauer et al. (2013) (R_N = 23 ± 7.5 km) and Schambeau et al. (2021) (R_N = 32.3 ± 3.1 km) that are based on *WISE* and *Spitzer* observations, respectively.

6.3. Thermal emission of the dust coma

The coma modeling of the 70 μm images yields measurements of the thermal flux emitted from the coma dust grains. We performed aperture photometry to each of the three datasets and provide the results in Table 7. Our approach for separating the nucleus versus coma flux from the 160 μm data was to calculate the expected 160-μm NEATM nucleus flux density for each of the three epochs of PACS images using the nucleus radius derived from the 70 μm data (see Table 7), and to subtract it from the individual 160 μm images. The residual flux density after subtraction was attributed to the dust coma and the three values are presented in Table 7. The extracted coma flux densities are for aperture radii of 10″ (2010 and 2013 data) and 6″ (2011 data). A source close to the nucleus of 29P is indeed observed in the 2 January 2011 image (Fig. 2).

Schambeau et al. (2021) measured the coma flux density of 29P at 16, 24, and 70 μm using *Spitzer* observations undertaken on 23–24 November 2003 (r_h = 5.73 au, Δ= 5.54 au). The uncertainty was large at 70 μm, but the measured value (102 ± 50 mJy in a 9″ radius aperture) is consistent with the *Herschel* measurements.

The 70 μm image obtained on 10 June 2010 is more extended that those obtained on 2 January 2011 and 17 February 2013 (Fig. 2). A possible explanation is the presence of residual ejecta from the May 2010 outbursts (E and F) and possibly from the more productive April 2010 outburst D (Tables 1 and 5). These outbursts occurred between 17 to 46 days before the acquisition of the 10 June 2010 image, whereas the two other PACS images were obtained more than 42 and 84 days after a significant out-
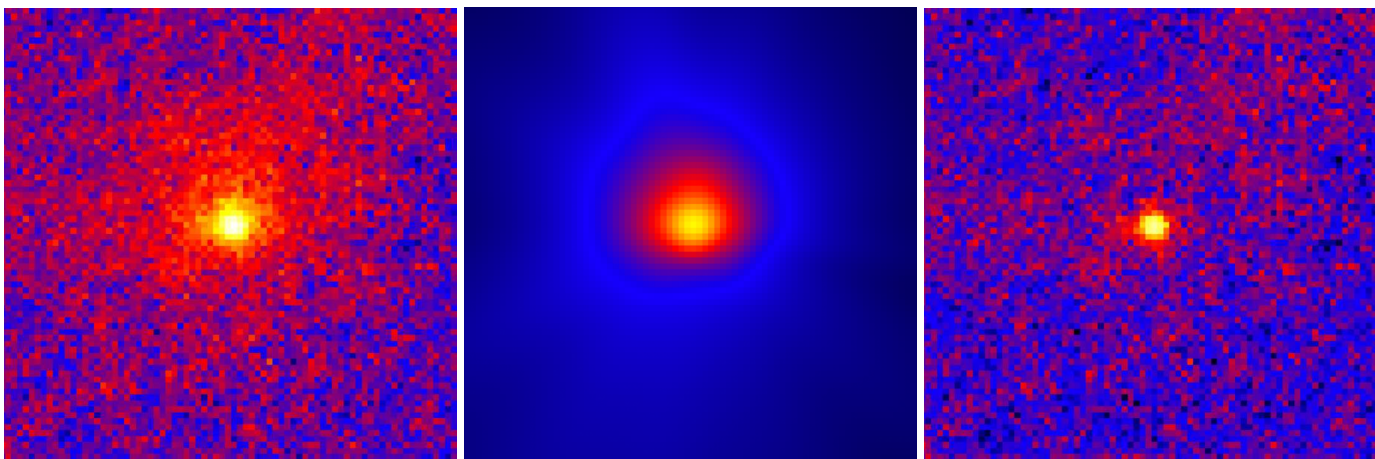
Fig. 14. PACS image in the 60-85 μm band from June 10, 2010. From left to right: Observed image ($2' \times 2'$, 5.77×10^5 km per side; equatorial north is up and east is to the left), the coma model, and the residuals after the coma model was subtracted.

burst. The average size of the outermost isophote ($\sim 1.2\ 10^5$ km, Fig. 2, top left) implies projected dust velocities between 30–80 m/s, depending on which outburst is considered.

6.4. Dust production rate

To determine the dust production rate Q_{dust}, we followed the approach used by Schambeau et al. (2021) to analyze *Spitzer* observations of the dust coma of 29P (see their Sect. 3.1.3). We applied the same model parameters. In summary, the model computes the thermal emission of an ensemble of particles defined by its size distribution, which is described by a power law $n(a) \propto a^{\alpha}$, where α is the size index and the particle radius takes values from a_{min} to a_{max}. The maximum size that can be lifted from the surface of the nucleus of 29P is estimated to be a_{max} = 250 μm, for a CO-driven activity restricted to a cone with a half-angle of 45° and a total CO production rate of 4×10^{28} s^{-1} and a 30 km radius nucleus (Zakharov et al. 2018, 2021). The wavelength-dependent absorption coefficient and temperature of the dust particles was computed as a function of grain size using the Mie theory combined with an effective medium theory in order to consider mixtures of different materials following Bockelée-Morvan et al. (2017) (see also Appendix C.2). We considered the two icy mixtures studied by Schambeau et al. (2021): 1) a matrix of crystalline ice with inclusions of amorphous carbon, and 2) a matrix of amorphous carbon with inclusions of crystalline ice. For the two mixtures, the ice fraction by mass is $\sim 45\%$. The dust temperatures inferred for mixture 1 are very similar to those of the ice-poor (29% by mass) mixture considered in Sect. 5.2, whereas the grain temperatures for mixture 2 are intermediate between the temperatures of ice-rich and ice-poor grains shown in Fig. 11. The dust density is taken equal to 500 kg/m^3. The dust velocity as a function of particle size varies $\propto a^{-0.5}$, with a value of 60 m/s for 10-μm particles. The model output is the coma flux density for a given circular aperture and wavelength.

In Table 8 we present Q_{dust} values derived from the measured 70 μm flux densities. Only results for particles made of amorphous carbon with inclusions of crystalline ice are given, because very similar results are obtained for the other icy mixture. The values in Col.1 provide results for a range of a_{min} and size index. In Col. 2, only the size distributions providing a flux density ratio F_{70}/F_{160} consistent with the observations (taking into account the large uncertainties at 160 μm) are considered.

Here, F_{70} and F_{160} refer to the measured coma flux density at 70 and 160 μm, respectively. In Col. 3, we use the size distributions consistent with the flux density ratio F_{16}/F_{24} measured by *Spitzer* (Schambeau et al. 2021). The range of inferred dust production rates is similar for these three cases because the dust size distribution is poorly constrained by the *Spitzer* and *Herschel* data. For shallow size distributions, the derived Q_{dust} values are strongly dependent on the assumed maximum particle size. For example, the upper range of Q_{dust} values in Table 8 is increased by 50% when we assume $a_{max} = 500\ \mu$m.

The dust production rates measured from the *Herschel* 2010 and 2011 data (~ 60–120 kg s^{-1}) are similar to the values derived from the *Spitzer* 2003 data (Schambeau et al. 2021). However, the PACS data indicate that comet 29P was a factor of 2.5 less productive in dust at the time of the 2013 *Herschel* observation. This low dust activity is not observed in the optical data. 29P was in a quiescent state during the three *Herschel*/PACS measurements with very similar nuclear magnitudes (Table 1).

7. SPIRE data

The images obtained on 10 June 2010 with the SPIRE photometer show a marginal signal at the position of comet 29P, against a background that is crowded by astronomic sources (Fig. A.1). Based on the 70 μm PACS analysis (Sect. 6), the estimated thermal fluxes from the 29P nucleus in the SPIRE photometer bandpasses during the observations are 14 mJy (250 μm), 8 mJy (350 μm), and 4 mJy (500 μm). The dust fluxes, estimated from the coma PACS 70μm fluxes measured on the same date are 16 (250 μm), 11 (350 μm), and 7 mJy/beam (500 μm). The expected nucleus+coma fluxes are accordingly 30, 19, and 11 mJy/beam at 250, 350, and 500 μm respectively. The measured signals at the position of the comet are 27.3±9.0, 9.0±7.5 and 9.0±10.8 mJy/beam at 250, 350 and 500 μm, respectively (we did not apply any color corrections). Therefore, this is consistent with the predictions. We have also to take into consideration the confusion limit of 5.8, 6.3, and 6.8 mJy/beam, at 250, 350 and 500 μm, respectively.

8. Summary

Comet 29P is a fascinating object for understanding distant cometary activity and evolutionary processes that affect the sur-

Table 7. PACS photometry results.

UT Date (yyyy/mm/dd)	70-μm Nuc. Flux[a] (mJy)	160-μm Nuc. Flux[b] (mJy)	NEATM Nuc. Radius (km)	70-μm Coma Flux[c] (mJy)	160-μm Coma Flux[c] (mJy)
2010/06/10	102 ± 10	31	30.8 ± 3	146 ± 10 (10″)	45 ± 10 (10″)
2011/01/02	128 ± 10	39	30.3 ± 3	93 ± 10 (6″)	36 ± 10 (6″)
2013/02/17	140 ± 10	43	31.9 ± 3	71 ± 10 (10″)	14 ± 5 (10″)

[a] The aperture-corrected total nucleus flux density measured in PACS 70-μm images. [b] 160 μm NEATM derived nucleus flux estimate based on the best-fit nucleus radius value derived from the 70 μm image analysis. [c] The radius of the photometric aperture is specified in brackets. The 2011 data used a smaller aperture due to the presence of a source close to the nucleus.

Table 8. Dust production rates.

UT Date (yyyy/mm/dd)	Dust Production rate (kg s^{-1})		
	(1)	(2)	(3)
2010/06/10	67–116	75–115	72–100
2011/01/02	58–108	66–107	67–93
2013/02/17	27–49	27–45	30–42

Note: Results for dust particles made of a matrix of amorphous carbon with inclusions of crystalline ice, with an ice content of 45% in mass. Column (1): Range of dust production rates inferred from the flux density at 70 μm for a_{min} = 0.5 to 10 μm, size index α from –4.5 to –2.5, and a_{max} = 250 μm. Column (2): Same as (1), but for a_{min} and α values providing a 70 μm to 160 μm flux density ratio F_{70}/F_{160} consistent with the observations. Column (3): Same as (1), but for a_{min} and α values providing a 16 μm to 24 μm flux density ratio F_{16}/F_{24} consistent with the *Spitzer* observations undertaken on 23–24 November 2003 (Schambeau et al. 2021).

face and interior of Centaurs. Its distant orbit makes investigations of the composition of its atmosphere quite challenging.

We used the HIFI and PACS instruments of the *Herschel* space observatory to observe the H_2O $1_{10}-1_{01}$ (557 GHz) and the NH_3 1_0-0_0 (573 GHz) lines, and to image the coma at 70 and 160 μm. *Herschel*/SPIRE images at 250, 350 and 500 μm were also acquired. Observations with the IRAM 30 m telescope were performed to monitor the CO production rate Q(CO) and to search for HCN, including at the time of the H_2O observations. HIFI and IRAM observations were performed soon after outbursts or during quiescent states. The following main results were obtained:

– CO production rates in the range $(2.9$–$5.6) \times 10^{28}$ s^{-1} (1400–2600 kg s^{-1}) are measured.

– A correlation between the CO production rate and dust brightness is observed (i.e., a higher CO production rate when the coma brightness is higher, e.g., at time of outbursts), with a regression slope between $\log_{10}(Q$(CO)) and the reduced nuclear magnitude $m_R(1, r_h, 0)$ equal to –0.062. During the quiescent states, the CO production rate is $\sim 3.0 \times 10^{28}$ s^{-1} (1400 kg s^{-1}). From the comparison with Hale-Bopp activity at 6 au from the Sun, we showed that the dust activity of 29P (but not the gas activity) is quenched in the regions responsible for the quiescent activity, likely as a result of surface evolutionary processes induced by activity.

– We found a correlation between the excess of CO production and the excess of dust brightness with respect to quiescent values. The correlation equation ($\log_{10}(Q_{out}$(CO) = $29.98 - 0.17 m_{R,out}(1, r_h, 0)$, considering IRAM data) is close to that established for the continuous activity of comet Hale-Bopp. This is consistent with a similar dust-to-gas flux ratio in the outburst ejecta of 29P and in the coma of Hale-Bopp (referring to dust particles that contribute to the scattering cross-section).

– The similarity of the CO line profiles during outburst and quiescent phases confirms that outbursts occur in the subsolar region, where CO outgassing predominantly and continuously operates.

– The water line was detected on 19 April and 11 May 2010. Assuming near-nucleus production, the derived production rates Q(H_2O) are $(4.6 \pm 0.8) \times 10^{27}$ s^{-1} and $(3.5 \pm 0.9) \times 10^{27}$ s^{-1}, respectively (about 120 kg s^{-1}). The mean Q(H_2O)/Q(CO) ratio is $10.0 \pm 1.5\%$ and is similar to the value derived from *Akari* infrared data. The water line was not detected on 30 December 2010, and the derived 3-σ upper limit is Q(H_2O)/Q(CO) < 8%.

– HCN is identified for the first time in the atmosphere of 29P. The relative production rates for the April-May 2010 period are Q(HCN)/Q(CO) = (0.12 ± 0.03)% and Q(HCN)/Q(H_2O) = (1.2 ± 0.3)% on average. The HCN abundance relative to water is a factor of 10 higher than values found in comets at 1 au the Sun.

– NH_3 was not detected. The derived 3-σ upper limit for the average of April and May 2010 data is 4.5×10^{27} s^{-1}, leading to Q(NH_3)/Q(CO) < 10% and Q(NH_3)/Q(H_2O) < 110%.

– The H_2O and HCN lines are narrow and symmetric in the comet rest velocity frame, and strongly differ in shape from the CO line. The small (at most) velocity offset observed for the H_2O and HCN lines indicates that the nucleus contributes little to the production of these molecules which are instead released from sublimating icy grains. The characteristics of the H_2O and HCN line profiles suggest that they are produced from dust particles that exceed a few micrometers in size.

– The H_2O observations of 19 April 2010 and 11 May 2010 were obtained a few days to a few weeks after the major outburst D of 16.8 April 2010. Assuming an outburst duration of two days, a size index $\alpha = -3.5$, and a maximum particle size of 50 μm in the dust ejecta, we showed from modeling that the weak decrease in the H_2O signal that is observed between the two dates can be explained if water is sublimating from large (> 5–7 μm) icy carbon-grains, in line with the size constraints obtained from the H_2O line profile (> 4–6 μm). The lower limit for the mass of the icy ejecta is 2×10^4 kg/s, which corresponds to a dust-to-CO production rate ratio (in

mass) > 22 for the outburst. The calculations do not consider the minor outburst E that occurred on 5 May 2010. A conservative lower limit of the dust-to-CO production rate ratio of 1.6 was obtained by considering only the 19 April 2010 data.

– Despite different production mechanisms, H_2O and CO productions are correlated, as suggested by the constant ratio of H_2O/CO line areas.

– We analyzed the PACS 70 and 160-μm images to provide estimates of the thermal flux detected from the nucleus and the dust coma. For the 70-μm images, the relative contributions of the two components were extracted. The NEATM model applied to the measured nucleus 70-μm flux density allowed us to derive three independent estimates of the nucleus radius (on the order of 31 ± 3 km), which agree with recently published values based on *WISE* and *Spitzer* data (Bauer et al. 2013; Schambeau et al. 2021). This might suggest that 29P is an approximately spherical body.

– The SPIRE images show marginal detections of the 29P thermal continuum.

– We obtained three measurements of the dust production rate during the quiescent state. The dust mass-loss rate was estimated to be in the range 60–120 kg s^{-1} on 10 June 2010 and 2 January 2011, but a factor of 2.5 lower on 17 February 2013. The dust-to-gas production rate ratio in mass is thus < 0.1 during quiescent phases.

– An important finding of our study is the presence of strong local heterogeneities on the surface of 29P, with quenched dust activity from most of the surface, but not in outbursting regions.

In the near future, the James Webb space telescope will provide the opportunity to investigate the activity and atmospheric composition of comet 29P in unprecedented detail. Not only CO and water, but other species that possibly contribute to its distant activity will hopefully be revealed.

References

Agarwal, J., Della Corte, V., Feldman, P. D., et al. 2017, MNRAS, 469, s606. doi:10.1093/mnras/stx2386

A'Hearn, M. F., Belton, M. J. S., Delamere, W. A., et al. 2011, Science, 332, 1396

A'Hearn, M. F., Feaga, L. M., Keller, H. U., et al. 2012, ApJ, 758, 29

Bauer, J. M., Grav, T., Blauvelt, E., et al. 2013, ApJ, 773, 22. doi:10.1088/0004-637X/773/1/22

Beer, E. H., Podolak, M., & Prialnik, D. 2006, Icarus, 180, 473. doi:10.1016/j.icarus.2005.10.018

Biver, N. 1997, Ph.D. Thesis, University Paris 7

Biver, N., Bockelée-Morvan, D., Crovisier, J., et al. 1999, AJ, 118, 1850

Biver, N., Bockelée-Morvan, D., Colom, P., et al. 2002, Earth Moon and Planets, 90, 5

Biver, N., Bockelée-Morvan, D., Crovisier, J., et al. 2007, Planet. Space Sci., 55, 1058. doi:10.1016/j.pss.2006.11.010

Biver, N., Bockelée-Morvan, D., Wiesemeyer, H., et al. 2008, Asteroids, Comets, Meteors 2008, 1405, 8146

Biver, N., Crovisier, J., Bockelée-Morvan, D., et al. 2012, A&A, 539, A68

Bocchio, M., Bianchi, A., & Abergel, S. 2016, VizieR Online Data Catalog, J/A+A/591/A117

Bockelée-Morvan, D., Crovisier, J., Mumma, M. J., & Weaver, H. A. 2004, Comets II, 391

Bockelée-Morvan, D., Biver, N., Crovisier, J., et al. 2010, Bull. Amer. Astron. Soc. 42, 946

Bockelée-Morvan, D., Hartogh, P., Crovisier, J., et al. 2010, A&A, 518, L149. doi:10.1051/0004-6361/201014655

Bockelée-Morvan, D., Biver, N., Swinyard, B., et al. 2012, A&A, 544, L15. doi:10.1051/0004-6361/201219744

Bockelée-Morvan, D., Biver, N., Crovisier, J., et al. 2014, A&A, 562, A5. doi:10.1051/0004-6361/201322939

Bockelée-Morvan, D., Rinaldi, G., Erard, S., et al. 2017, MNRAS, 469, S443. doi:10.1093/mnras/stx1950

Cochran, A. L., & Cochran, W. D. 1991, Icarus, 90, 172

Cowan, J. J. & A'Hearn, M. F. 1979, Moon and Planets, 21, 155. doi:10.1007/BF00897085

Crifo, J. F. & Rodionov, A. V. 1997, Icarus, 127, 319. doi:10.1006/icar.1997.5690

Crifo, J. F., Rodionov, A. V., & Bockelée-Morvan, D. 1999, Icarus, 138, 85

Crovisier, J., Biver, N., Bockelée-Morvan, D., et al. 1995, Icarus, 115, 213

Davies, J. K., Roush, T. L., Cruikshank, D. P., et al. 1997, Icarus, 127, 238

de Graauw, Th., Helmich, F.P., Phillips, T.G., et al. 2010, A&A, 518, L6

Dello Russo, N., Kawakita, H., Vervack, R. J., et al. 2016, Icarus, 278, 301. doi:10.1016/j.icarus.2016.05.039

de Val-Borro, M., Hartogh, P., Crovisier, J., et al. 2010, A&A, 521, L50. doi:10.1051/0004-6361/201015161

de Val-Borro, M., Bockelée-Morvan, D., Jehin, E., et al. 2014, A&A, 564, A124. doi:10.1051/0004-6361/201423427

DiSanti, M. A., Bonev, B. P., Russo, N. D., et al. 2017, AJ, 154, 246. doi:10.3847/1538-3881/aa8639

Dorschner, J., Begemann, B., Henning, T., Jaeger, C., & Mutschke, H. 1995, A&A, 300, 503

Edoh, J. H. 1983, Ph.D. thesis, Univ. Arizona

Enzian, A., Cabot, H., & Klinger, J. 1997, A&A, 319, 995

Exter, K., Balog, Z., Calzoletti, L., et al. 2018, The Photodetector Array Camera and Spectrometer (PACS) Handbook, Herschel-HSC-DOC-2101

Fanale, F. P., & Salvail, J. R. 1984, Icarus, 60, 476

Feldman, P. D., McPhate, J. B., Weaver, H. A., Tozzi, G.-P., & A'Hearn, M. F. 1996, Bulletin of the American Astronomical Society, 28, 1084

Fernandez, Y. R. 1999, Ph.D. Thesis, 6150

Fernández, Y. R., Kelley, M. S., Lamy, P. L., et al. 2013, Icarus, 226, 1138. doi:10.1016/j.icarus.2013.07.021

Festou, M. C., Gunnarsson, M., Rickman, H., Winnberg, A., & Tancredi, G. 2001, Icarus, 150, 140

Fornasier, S., Lellouch, E., Müller, T., et al. 2013, A&A, 555, A15

Fougere, N., Combi, M. R., Tenishev, V., et al. 2012, Icarus, 221, 174

Fray, N., & Schmitt, B. 2009, Planet. Space Sci., 57, 2053

Fulle, M. 1992, Nature, 359, 42

Greenberg, J. M.,& Hage, J. I. 1990, ApJ, 361, 260

Griffin, M. J., Abergel, A., Abreu, A., et al. 2010, A&A, 518, L3. doi:10.1051/0004-6361/201014519

Groussin, O., Sunshine, J. M., Feaga, L. M., et al. 2013, Icarus, 222, 580

Grün, E., Hanner, M. S., Peschke, S. B., et al. 2001, A&A, 377, 1098. doi:10.1051/0004-6361:20011139

Gulkis, S., Allen, M., von Allmen, P., et al. 2015, Science, 347, aaa0709

Gunnarsson, M., Rickman, H., Festou, M. C., Winnberg, A., & Tancredi, G. 2002, Icarus, 157, 309

Gunnarsson, M. 2003, A&A, 398, 353

Gunnarsson, M., Bockelée-Morvan, D., Biver, N., Crovisier, J., & Rickman, H. 2008, A&A, 484, 537

Harris, A. W. 1998, Icarus, 131, 291

Harris, A. W. & Lagerros, J. S. V. 2002, Asteroids III, 205

Hartogh, P., Lellouch, E., Crovisier, J. et al. 2009, P&SS, 57, 1596

Höfner, S., Vincent, J.-B., Blum, J., et al. 2017, A&A, 608, DA121. doi:10.1051/0004-6361/201628726

Hosek, M. W., Blaauw, R. C., Cooke, W. J., Suggs, R. M. 2013, AJ, 145, 122

Ivanova, O. V., Luk'yanyk, I. V., Kiselev, N. N., et al. 2016, Planet. Space Sci., 121, 10. doi:10.1016/j.pss.2015.12.001

Jehin, E., Gillon, M., Queloz, D., et al. 2011, The Messenger, 145, 2

Kawakita, H., Watanabe, J.-i., Ootsubo, T., et al. 2004, ApJ, 601, L191

Korsun, P. P., Ivanova, O. V., & Afanasiev, V. L. 2008, Icarus, 198, 465

Kossacki, K. J., & Szutowicz, S. 2013, Icarus, 225, 111

Lamy, P. L. & Toth, I. 1995, A&A, 293, L43

Lellouch, E., Crovisier, J., Lim, T., et al. 1998, A&A, 339, L9

Lellouch, E., Santos-Sanz, P., Lacerda, P., et al. 2013, A&A, 557, A60

Lippi, M., Villanueva, G. L., Mumma, M. J., et al. 2021, AJ, 162, 74. doi:10.3847/1538-3881/abfdb7

Lis, D. C., Bockelée-Morvan, D., Güsten, R., et al. 2019, A&A, 625, L5. doi:10.1051/0004-6361/201935554

Lisse, C. M., Fernández, Y. R., Kundu, A., et al. 1999, Icarus, 140, 189. doi:10.1006/icar.1999.6131

Marshall, D., Groussin, O., Vincent, J.-B., et al. 2018, A&A, 616, A122

Miles, R. 2016, Icarus, 272, 387. doi:10.1016/j.icarus.2015.11.011

Naves, R., & Campàs, M. 2007, MPEC 2007-Y59, http://www.observadores-cometas.com

Ootsubo, T., Kawakita, H., Hamada, S., et al. 2012, ApJ, 752, 15

Paganini, L., Mumma, M. J., Boehnhardt, H., et al. 2013, ApJ, 766, 100

Pajola, M., Höfner, S., Vincent, J. B., et al. 2017, Nature Astronomy, 1, 0092. doi:10.1038/s41550-017-0092

Pilbratt, G. L., Riedinger, J. R., Passvogel, T., et al. 2010, A&A, 518, L1

Poglitsch, A., Waelkens, C., Geis, N., et al. 2010, A&A, 518, L2

Prialnik, D. & Bar-Nun, A. 1987, ApJ, 313, 893. doi:10.1086/165029

Prialnik, D. & Bar-Nun, A. 1990, ApJ, 363, 274. doi:10.1086/169339

Protopapa, S., Sunshine, J. M., Feaga, L. M., et al. 2014, Icarus, 238, 191

Protopapa, S., Kelley, M. S. P., Yang, B., et al. 2018, ApJ, 862, L16

Sarid, G., Volk, K., Steckloff, J. K., et al. 2019, ApJ, 883, L25. doi:10.3847/2041-8213/ab3fb3

Schambeau, C. A., Fernández, Y. R., Lisse, C. M., et al. 2015, Icarus, 260, 60

Schambeau, C. A., Fernández, Y. R., Samarasinha, N. H., et al. 2017, Icarus, 284, 359. doi:10.1016/j.icarus.2016.11.026

Schambeau, C. A., Fernández, Y. R., Samarasinha, N. H., et al. 2021, PSJ, 2, 126. doi:10.3847/PSJ/abfe6f

Schleicher, D. G. 2009, AJ, 138, 1062. doi:10.1088/0004-6256/138/4/1062

Schleicher, D. G. & Bair, A. N. 2011, AJ, 141, 177. doi:10.1088/0004-6256/141/6/177

Senay, M. C., & Jewitt, D. 1994, Nature, 371, 229

Shipman, R. F., Beaulieu, S. F., Teyssier, D., et al. 2017, A&A, 608, A49

Stansberry, J. A., Van Cleve, J., Reach, W. T., et al. 2004, ApJS, 154, 463

Swinyard, B. M., Ade, P., Baluteau, J.-P., et al. 2010, A&A, 518, L4. doi:10.1051/0004-6361/201014605

Szabó, G. M., Kiss, L. L., Pál, A., et al. 2012, ApJ, 761, 8. doi:10.1088/0004-637X/761/1/8

Tenishev, V., Combi, M., & Davidsson, B. 2008, ApJ, 685, 659. doi:10.1086/590376

Teyssier, D., Avruch, I., Beaulieu, S., et al. 2017, HIFI Handbook, HERSCHEL-HSC-DOC-2097

Trigo-Rodríguez, J. M., García-Melendo, E., Davidsson, B. J. R., et al. 2008, A&A, 485, 599

Trigo-Rodríguez, J. M., García-Hernández, D. A., Sánchez, A., et al. 2010, MN-RAS, 409, 1682

Tubiana, C., Rinaldi, G., Güttler, C., et al. 2019, A&A, 630, A23. doi:10.1051/0004-6361/201834869

Valchanov, I. 2017, Herschel Explanatory Supplement vol. IV, HERSCHEL-HSC-DOC-0798

Vincent, J.-B., A'Hearn, M. F., Lin, Z.-Y., et al. 2016, MNRAS, 462, S184. doi:10.1093/mnras/stw2409

Vincent, J.-B., Oklay, N., Pajola, M., et al. 2016, A&A, 587, A14. doi:10.1051/0004-6361/201527159

Warren, S. G., & Brandt, R. E. 2008, JGR 113, D14220

Weiler, M., Rauer, H., Knollenberg, J., et al. 2003, A&A, 403, 313. doi:10.1051/0004-6361:20030289

Wierzchos, K. & Womack, M. 2020, AJ, 159, 136

Womack, M., Curtis, O., Rabson, D. A., et al. 2021, PSJ, 2, 17. doi:10.3847/PSJ/abd32c

Zakharov, V., Bockelée-Morvan, D., Biver, N., Crovisier, J., & Lecacheux, A. 2007, A&A, 473, 303

Zakharov, V. V., Ivanovski, S. L., Crifo, J.-F., et al. 2018, Icarus, 312, 121. doi:10.1016/j.icarus.2018.04.030

Zakharov, V. V., Rodionov, A. V., Fulle, M., et al. 2021, Icarus, 354, 114091. doi:10.1016/j.icarus.2020.114091

Appendix A: SPIRE images
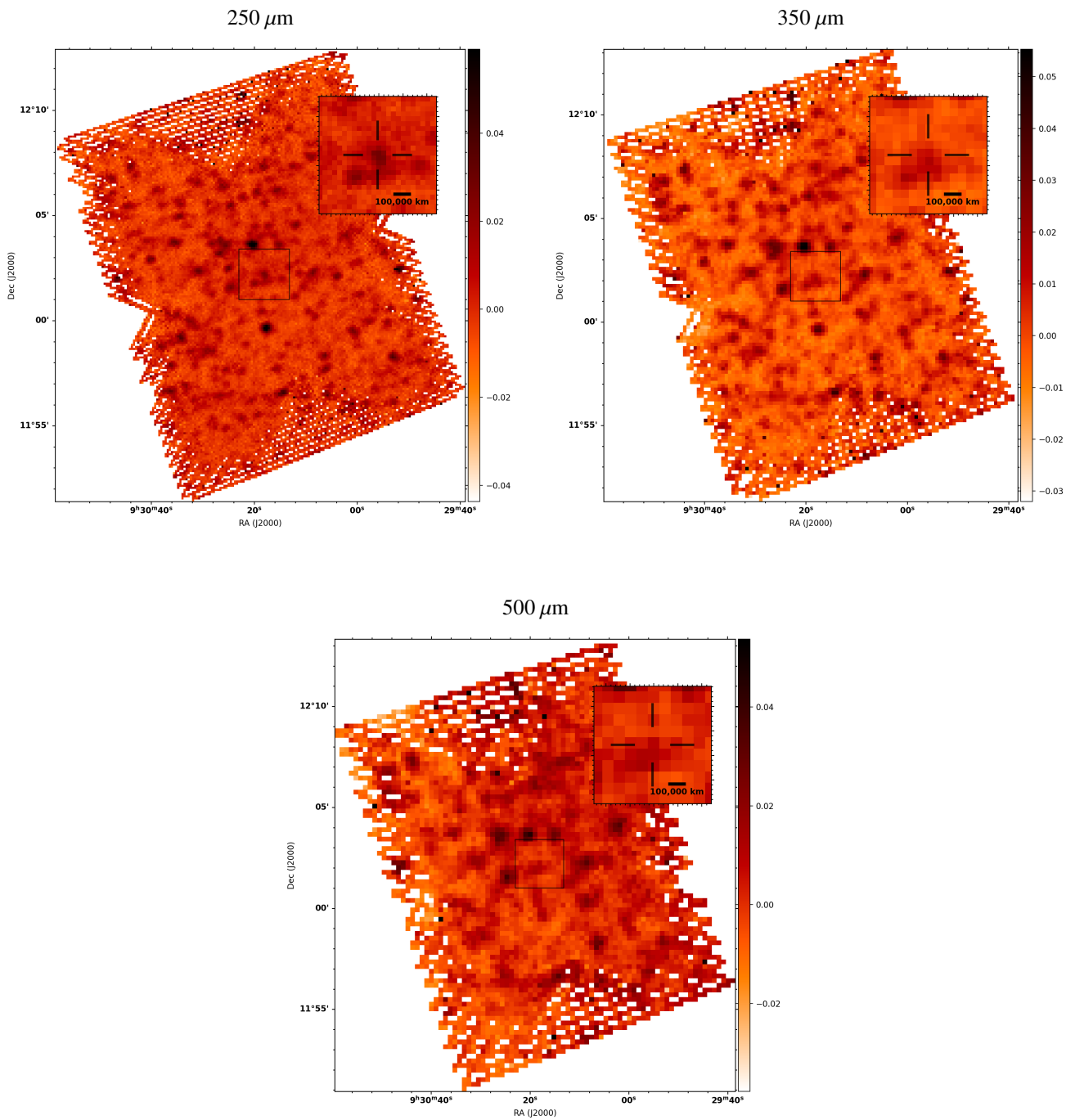
Fig. A.1. SPIRE images of 29P in 250 (top left), 350 (top right) and 500 (bottom) μm filters obtained on 10 June 2010. Flux is given in Jy/beam (color bar). The insets show a zoom of the images centered on the comet position. Negative pixel values are the result of the local background subtraction.

Appendix B: C/1995 O1 (Hale-Bopp): Correlation between nuclear magnitude and CO production rate

Womack et al. (2021) presented correlation equations between visual magnitudes and CO production rates for comet C/1995 O1 (Hale-Bopp),

$$
\begin{aligned}
\log_{10}(Q(CO)) &= 29.9 - 0.24 m_h \\
&= 29.9 - 0.24(m_v - 5\log_{10}(\Delta)),
\end{aligned} \tag{B.1}
$$

where m_h is the heliocentric magnitude, and m_v is the total visual magnitude. A slightly different correlation is found when a phase correction is applied to the magnitudes (as done in Sect. 2.5 for 29P) and systematic differences between observers are corrected, (Womack et al. 2021)

$$
\log_{10}(Q(CO)) = 29.71 - 0.22 m_{shift}. \tag{B.2}
$$

For 29P, the correlation equation for 29P involves the nuclear magnitude. An additional correction factor must therefore be applied to Eq. B.2 to compare the correlations of 29P and Hale-Bopp (nuclear magnitudes are not available for Hale-Bopp).

For a steady-state dust production, assuming a $1/\rho$ decrease in coma brightness with projected distance ρ from comet center, the integrated magnitude in an aperture of radius ρ varies as

$$
m(\rho) = m(\rho_0) - 2.5\log_{10}(\frac{\rho}{\rho_0}). \tag{B.3}
$$

At a distance of ≈ 6 au from the Sun, in October–November 1995 and July–September 1998, the Hale-Bopp coma was 2–3′ in diameter, so that we estimate that the nuclear magnitudes in a 10″ diameter aperture should have been $+3 \pm 0.2$ magnitude fainter than the total magnitudes m_v used for the correlation with the CO production rate (on the other hand, when the comet was twice as close to the Sun and Earth its coma was 10±5′ in diameter, and the nuclear magnitude in a 20″ diameter aperture should have been about 3.5±0.6 magnitudes fainter than m_v). As a consequence the correlation between Q_{CO} and total heliocentric magnitudes for Hale-Bopp (Eq. B.3 can approximately be extrapolated to a correlation with nuclear heliocentric magnitudes (within an aperture diameter of ~10″) by adding $+0.8\pm0.2$ to the constant parameter,

$$
\log_{10}(Q(CO)) = 30.5(\pm0.2) - 0.22 m_R(1, r_h, 0). \tag{B.4}
$$

At 6 au from the Sun, the total visual magnitude corrected from geocentric distance and phase of comet Hale-Bopp was ~ 6 (Wierzchos & Womack 2020), so that $m_R(1, r_h, 0)$ at 6 au is estimated to ~ 9.

Appendix C: Dust models

C.1. Dust velocity

The dust velocity as a function of grain radius a is computed following Crifo & Rodionov (1997),

$$
v_a = \frac{v_g}{1.2 + 0.72(a/a^*)^{0.5}} \tag{C.1}
$$

with

$$
a^* = \frac{m_{CO}\, Q_e(CO)}{4\pi\, r_N\, \rho_d\, v_{g0}}, \tag{C.2}
$$

where v_g is the CO terminal velocity, taken equal to 0.5 km s^{-1} (i.e. similar to the value measured in the jet component of the CO spectrum), and v_{g0} is the CO velocity at the nucleus surface,

$$
v_{g0} = \sqrt{\frac{\gamma_{CO} k_B T_N}{m_{CO}}}. \tag{C.3}
$$

r_N and T_N are the nucleus radius and temperature (assumed to be 30 km and 160 K for 29P). ρ_d is the dust density, taken equal to 500 kg m^{-3} to calculate the velocity of dust grains (Fig.11) and dust production rate (Sect. 6.4). γ_{CO} is the heat capacity ratio of CO (= 1.4), m_{CO} is the mass of one CO molecule, and $Q_e(CO)$ is the equivalent CO production rate defined as $Q_e(CO) = Q(CO) \times 4\pi/\Omega$, where Ω is the solid angle of the jet and $Q(CO)$ is the total production rate.

C.2. Grain composition and temperature

Icy grains are modeled as constituted of a matrix of crystalline ice incorporating impurities (silicates or carbon). The relative fractions of each component are defined by the fractional volume of impurities (also referred to as dirt) v_i with respect to the total volume of the grain. The total ice content by mass is computed assuming densities of 1000 kg m^{-3} and 2500 kg m^{-3} for ice and impurities, respectively, and a grain porosity $p = 0.5$. We consider in this paper values of v_i of 0.1, and 0.5, dirt-to-ice mass ratios of 0.28, and 2.5, respectively. For v_i of 0.1 and 0.5, the ice mass fraction is thus 78% and 29%, respectively

The grain temperatures were computed assuming radiative equilibrium. At 6 au from the Sun, grain temperatures are low, and cooling by sublimation is negligible with respect to thermal radiation (Gunnarsson 2003; Beer et al. 2006). The energy balance involves grain absorption coefficients Q_{abs}, which were computed using the Mie theory. Refractive indices for mixtures were obtained from the Maxwell-Garnett effective medium theory following Greenberg & Hage (1990). The Maxwell-Garnett effective medium theory was also used to compute refractive indices of porous grains. Refractive indices for silicates (namely olivine with 50% Mg and 50% Fe), carbon, and ice were taken from Dorschner et al. (1995), Edoh (1983), and Warren & Brandt (2008), respectively. More details on the model can be found in Bockelée-Morvan et al. (2017).

C.3. Grain sublimation

The sublimation of dirty icy grains results in an ice mass loss,

$$
\frac{dm_{ice}}{dt} = -(1 - v_i)4\pi a^2 Z_{H_2O} m_{H_2O} \tag{C.4}
$$

where m_{H_2O} is the mass of one water molecule. We assumed that ice and impurities are intimately and homogeneously mixed. Therefore, the surfacic fraction of the ice is equal to the ice volumic fraction of $1 - v_i$. Z_{H_2O} is the water sublimation rate by unit of time and surface (m^{-2} s^{-1}), derived from the vapor pressure law of Fanale & Salvail (1984), which depends on the grain temperature T_d,

$$
Z_{H_2O} = A e^{-B/T_d} \sqrt{\frac{1}{2\pi m_{H_2O} k_B T_d}}, \tag{C.5}
$$

with $A = 3.56\ 10^{12}$ Pa, and $B = 6141.667$ K. The temperature of the dust particles as a function of size was computed as described in Sect. C.2.

The variation of the grain radius with time follows

$$\frac{da}{dt} = -\frac{Z_{H_2O} m_{H_2O}}{\rho_d} \qquad (C.6)$$

where ρ_d is the grain density: 575 and 875 kg m^{-3}, for ice-rich (v_i = 0.1) and ice-poor (v_i = 0.5) grains, respectively, for a porosity of 0.5. To compute the sublimation rate of the grains as a function of time, and initial size, we took into account that grains become hotter when their size diminishes due to sublimation. The impurities embedded in the ice are released together with the gas as it sublimates. Sublimation stops when water ice is exhausted. This defines the grain-sublimation lifetime. Similar approaches were used by Gunnarsson (2003) and Beer et al. (2006).

C.4. Dynamics and number density of water molecules sublimated from grains

In order to interpret the number of water molecules detected within the HIFI beam (Sect. 5.3), it is requisite to describe the dynamics of the water molecules sublimated from grains.

Our model assumes that, when they are released from grains, H_2O molecules expand radially outward in the coma at a velocity equal to v_{H_2O} = 0.25 km s^{-1}. This corresponds to the H_2O velocity derived from the width of the H_2O 557 GHz line profile (Sect. 2.1).

The distance traveled by the molecules at time t is given by

$$l = v_a(t_a - t_0) + v_{H_2O}(t - t_a) \qquad (C.7)$$

where t_0 is the time at which the grain is released from the nucleus, and t_a is the time at which the molecule sublimates. v_a is the dust velocity defined in Sect. C.1. The number of molecules sublimating at t_a from grains of radius a is derived from the ice mass-loss rate (Eq. C.4).

The algorithm was adapted to simulate an outburst described by a boxcar function with the outburst duration as a free parameter. The injected dust particles follow a size distribution. For comparison with the observations, the algorithm computes the water distribution at an elapsed time with respect to outburst onset (at t = 0 s). This was done by computing the number of molecules within spheres of increasing radius (nominally 40 spheres with radii from 10^3 to 10^7 km, with a logarithmic step). The number density (m^{-3}) throughout the coma can then easily be deduced. The expanding dust and H_2O clouds were assumed to be isotropic. The number of molecules within the HIFI beam was computed by volume integration.

Appendix D: Magnitude data

Table D.1. Magnitudes in an aperture with a diameter of 10″ in 2007–2008.

Date jj/mm/yyyy	Time hr:mn	Obs[a]	r_h (au)	Δ (au)	m_R	$m_R(1, r_h, 0)$	Date jj/mm/yyyy	Time hr:mn	Obs	r_h (au)	Δ (au)	m_R	$m_R(1, r_h, 0)$
24/12/2007	23:05	442	5.979	5.003	16.12	12.57	30/12/2007	00:13	J46	5.981	5.010	12.95	9.38
25/12/2007	21:10	442	5.980	5.003	16.00	12.45	30/12/2007	00:14	J46	5.981	5.010	12.96	9.39
25/12/2007	21:18	213	5.980	5.003	15.90	12.35	30/12/2007	00:15	J46	5.981	5.010	12.95	9.38
25/12/2007	21:24	213	5.980	5.003	15.88	12.33	30/12/2007	00:16	J46	5.981	5.010	12.96	9.39
25/12/2007	21:25	213	5.980	5.003	15.90	12.35	30/12/2007	00:17	J46	5.981	5.010	12.96	9.39
25/12/2007	21:29	213	5.980	5.003	15.90	12.35	30/12/2007	00:18	J46	5.981	5.010	12.95	9.38
26/12/2007	23:04	442	5.980	5.004	16.06	12.51	30/12/2007	00:19	J46	5.981	5.010	12.95	9.38
27/12/2007	19:28	J36	5.980	5.006	15.80	12.24	30/12/2007	00:20	J46	5.981	5.010	12.95	9.38
27/12/2007	19:36	J36	5.980	5.006	15.83	12.27	30/12/2007	00:21	J46	5.981	5.010	12.92	9.35
27/12/2007	19:37	J36	5.980	5.006	15.80	12.24	30/12/2007	00:22	J46	5.981	5.010	12.96	9.39
27/12/2007	19:47	J36	5.980	5.006	15.80	12.24	30/12/2007	00:23	J46	5.981	5.010	12.95	9.38
27/12/2007	19:53	J76	5.980	5.006	16.00	12.44	30/12/2007	00:24	J46	5.981	5.010	12.95	9.38
27/12/2007	19:58	J76	5.980	5.006	16.00	12.44	30/12/2007	00:25	J46	5.981	5.010	12.94	9.37
27/12/2007	19:59	J76	5.980	5.006	15.97	12.41	30/12/2007	00:26	J46	5.981	5.010	12.95	9.38
27/12/2007	20:04	J76	5.980	5.006	16.00	12.44	30/12/2007	00:27	J46	5.981	5.010	12.93	9.36
27/12/2007	20:16	213	5.980	5.006	15.90	12.34	30/12/2007	00:28	J46	5.981	5.010	12.95	9.38
27/12/2007	20:23	213	5.980	5.006	15.91	12.35	30/12/2007	00:29	J46	5.981	5.010	12.94	9.37
27/12/2007	20:23	213	5.980	5.006	15.90	12.34	30/12/2007	00:30	J46	5.981	5.010	12.95	9.38
27/12/2007	20:31	213	5.980	5.006	15.90	12.34	30/12/2007	00:31	J46	5.981	5.010	12.92	9.35
28/12/2007	20:02	J46	5.980	5.007	15.80	12.24	30/12/2007	00:32	J46	5.981	5.010	12.90	9.33
28/12/2007	20:11	J46	5.980	5.007	15.80	12.24	30/12/2007	17:51	B20	5.981	5.012	13.00	9.43
28/12/2007	20:58	J47	5.980	5.007	15.90	12.34	30/12/2007	17:54	B20	5.981	5.010	13.05	9.48
28/12/2007	21:11	J47	5.980	5.007	15.90	12.34	30/12/2007	17:54	B20	5.981	5.012	13.10	9.53
28/12/2007	21:11	J47	5.980	5.007	15.90	12.34	30/12/2007	17:58	B20	5.981	5.012	13.10	9.52
28/12/2007	21:24	J47	5.980	5.007	15.90	12.34	30/12/2007	18:03	213	5.981	5.012	12.90	9.32
28/12/2007	22:37	J38	5.980	5.007	15.80	12.24	30/12/2007	18:05	213	5.981	5.012	13.00	9.42
28/12/2007	22:40	J38	5.980	5.007	15.80	12.24	30/12/2007	18:06	213	5.981	5.010	12.97	9.40
28/12/2007	22:43	J38	5.980	5.007	15.70	12.14	30/12/2007	18:10	213	5.981	5.012	13.00	9.42
28/12/2007	22:48	J38	5.980	5.007	15.80	12.24	30/12/2007	19:55	J46	5.981	5.010	12.95	9.38
28/12/2007	23:17	A06	5.980	5.007	15.90	12.34	30/12/2007	20:03	170	5.981	5.012	13.00	9.42
28/12/2007	23:21	A06	5.980	5.007	15.89	12.33	30/12/2007	20:21	442	5.981	5.010	13.06	9.49
28/12/2007	23:28	A06	5.980	5.007	15.90	12.34	30/12/2007	21:08	X10	5.981	5.012	13.10	9.52
28/12/2007	23:44	A06	5.980	5.007	15.90	12.34	30/12/2007	21:12	X10	5.981	5.012	13.10	9.52
29/12/2007	21:51	213	5.981	5.010	14.00	10.43	30/12/2007	21:13	X10	5.981	5.010	13.09	9.52
29/12/2007	21:56	213	5.981	5.010	13.80	10.23	30/12/2007	21:17	X10	5.981	5.012	13.10	9.52
29/12/2007	22:06	213	5.981	5.010	13.84	10.27	30/12/2007	21:25	X10	5.981	5.012	13.10	9.52
29/12/2007	22:13	213	5.981	5.010	13.78	10.21	30/12/2007	21:50	J36	5.981	5.012	12.90	9.32
29/12/2007	22:38	J46	5.981	5.010	13.41	9.84	30/12/2007	22:00	J36	5.981	5.010	12.96	9.38
29/12/2007	22:39	J46	5.981	5.010	13.38	9.81	30/12/2007	22:10	J36	5.981	5.012	13.00	9.42
29/12/2007	22:40	J46	5.981	5.010	13.39	9.82	30/12/2007	22:11	J36	5.981	5.012	13.00	9.42
29/12/2007	22:41	J46	5.981	5.010	13.38	9.81	30/12/2007	23:19	J38	5.981	5.012	13.10	9.52
29/12/2007	22:42	J46	5.981	5.010	13.38	9.81	30/12/2007	23:21	A06	5.981	5.012	13.00	9.42
29/12/2007	22:43	J46	5.981	5.010	13.33	9.76	30/12/2007	23:22	J38	5.981	5.012	13.10	9.52
29/12/2007	22:44	J46	5.981	5.010	13.35	9.78	30/12/2007	23:25	J38	5.981	5.012	13.10	9.52
29/12/2007	22:45	J46	5.981	5.010	13.33	9.76	30/12/2007	23:27	J38	5.981	5.010	13.06	9.48
29/12/2007	22:46	J46	5.981	5.010	13.35	9.78	30/12/2007	23:27	A06	5.981	5.010	12.97	9.39
29/12/2007	22:48	J46	5.981	5.010	13.30	9.73	30/12/2007	23:40	A06	5.981	5.012	13.00	9.42
29/12/2007	22:49	J46	5.981	5.010	13.28	9.71	30/12/2007	23:58	A06	5.981	5.012	13.00	9.42
29/12/2007	22:50	J46	5.981	5.010	13.26	9.69	31/12/2007	01:03	945	5.981	5.012	13.00	9.42
29/12/2007	22:51	J46	5.981	5.010	13.26	9.69	31/12/2007	01:06	945	5.981	5.012	13.00	9.42
29/12/2007	22:52	J46	5.981	5.010	13.25	9.68	31/12/2007	01:09	945	5.981	5.012	13.10	9.52
29/12/2007	22:53	J46	5.981	5.010	13.23	9.66	31/12/2007	01:09	945	5.981	5.010	13.02	9.44
29/12/2007	22:55	J46	5.981	5.010	13.22	9.65	31/12/2007	01:12	945	5.981	5.012	13.10	9.52
29/12/2007	22:56	J46	5.981	5.010	13.23	9.66	31/12/2007	01:15	945	5.981	5.012	13.00	9.42
29/12/2007	22:57	J46	5.981	5.010	13.21	9.64	31/12/2007	21:46	J40	5.981	5.014	13.40	9.82
29/12/2007	22:58	J46	5.981	5.010	13.20	9.63	31/12/2007	21:47	J40	5.981	5.014	13.20	9.62
29/12/2007	22:59	J46	5.981	5.010	13.19	9.62	31/12/2007	21:49	J40	5.981	5.012	13.30	9.72
29/12/2007	23:00	J46	5.981	5.010	13.20	9.63	31/12/2007	21:54	J40	5.981	5.014	13.30	9.72
29/12/2007	23:01	J46	5.981	5.010	13.16	9.59	01/01/2008	03:15	213	5.982	5.017	13.20	9.61
29/12/2007	23:02	J46	5.981	5.010	13.16	9.59	01/01/2008	03:17	213	5.981	5.014	13.24	9.66
29/12/2007	23:03	J46	5.981	5.010	13.17	9.60	01/01/2008	03:20	213	5.982	5.017	13.30	9.71
29/12/2007	23:04	J46	5.981	5.010	13.14	9.57	01/01/2008	21:12	213	5.982	5.017	13.40	9.81

Continued on next page

Date jj/mm/yyyy	Time hr:mn	Obs	r_h (au)	Δ (au)	m_R	$m_R(1, r_h, 0)$	Date jj/mm/yyyy	Time hr:mn	Obs	r_h (au)	Δ (au)	m_R	$m_R(1, r_h, 0)$
29/12/2007	23:05	J46	5.981	5.010	13.15	9.58	01/01/2008	21:23	213	5.982	5.017	13.45	9.86
29/12/2007	23:06	J46	5.981	5.010	13.14	9.57	01/01/2008	21:33	213	5.982	5.017	13.40	9.81
29/12/2007	23:07	J46	5.981	5.010	13.11	9.54	01/01/2008	21:45	J51	5.982	5.017	13.00	9.41
29/12/2007	23:08	J46	5.981	5.010	13.10	9.53	01/01/2008	21:59	J51	5.982	5.017	13.00	9.41
29/12/2007	23:09	J46	5.981	5.010	13.11	9.54	01/01/2008	22:14	J51	5.982	5.017	12.90	9.31
29/12/2007	23:10	J46	5.981	5.010	13.10	9.53	02/01/2008	19:22	J46	5.982	5.021	13.68	10.08
29/12/2007	23:11	J46	5.981	5.010	13.10	9.53	02/01/2008	19:23	J46	5.982	5.021	13.68	10.08
29/12/2007	23:12	J46	5.981	5.010	13.11	9.54	02/01/2008	21:36	J51	5.982	5.021	13.80	10.20
29/12/2007	23:13	J46	5.981	5.010	13.08	9.51	02/01/2008	21:48	J51	5.982	5.021	13.80	10.20
29/12/2007	23:14	J46	5.981	5.010	13.11	9.54	02/01/2008	21:54	J51	5.982	5.021	13.77	10.17
29/12/2007	23:15	J46	5.981	5.010	13.09	9.52	02/01/2008	22:00	J51	5.982	5.021	13.80	10.20
29/12/2007	23:16	J46	5.981	5.010	13.07	9.50	02/01/2008	22:13	J51	5.982	5.021	13.80	10.20
29/12/2007	23:17	J46	5.981	5.010	13.07	9.50	03/01/2008	19:10	J38	5.982	5.024	14.00	10.39
29/12/2007	23:18	J46	5.981	5.010	13.07	9.50	03/01/2008	19:16	J38	5.982	5.024	14.00	10.39
29/12/2007	23:19	J46	5.981	5.010	13.06	9.49	03/01/2008	19:17	J38	5.982	5.024	13.99	10.38
29/12/2007	23:22	J46	5.981	5.010	13.04	9.47	03/01/2008	19:22	J38	5.982	5.024	14.00	10.39
29/12/2007	23:23	J46	5.981	5.010	13.04	9.47	03/01/2008	21:06	213	5.982	5.024	13.70	10.09
29/12/2007	23:24	J46	5.981	5.010	13.04	9.47	03/01/2008	21:15	213	5.982	5.024	13.84	10.23
29/12/2007	23:25	J46	5.981	5.010	13.03	9.46	03/01/2008	21:25	213	5.982	5.024	13.80	10.19
29/12/2007	23:26	J46	5.981	5.010	13.04	9.47	03/01/2008	21:28	213	5.982	5.024	13.90	10.29
29/12/2007	23:27	J46	5.981	5.010	13.03	9.46	03/01/2008	23:37	J46	5.982	5.024	13.89	10.28
29/12/2007	23:28	J46	5.981	5.010	13.02	9.45	06/01/2008	20:31	213	5.983	5.037	13.10	9.47
29/12/2007	23:30	J46	5.981	5.010	13.03	9.46	06/01/2008	20:35	213	5.983	5.037	13.11	9.48
29/12/2007	23:31	J46	5.981	5.010	13.00	9.43	06/01/2008	20:35	213	5.983	5.037	13.10	9.47
29/12/2007	23:32	J46	5.981	5.010	13.00	9.43	06/01/2008	20:39	213	5.983	5.037	13.10	9.47
29/12/2007	23:33	J46	5.981	5.010	13.00	9.43	06/01/2008	20:54	B20	5.983	5.037	13.18	9.55
29/12/2007	23:34	J46	5.981	5.010	13.01	9.44	06/01/2008	21:02	J51	5.983	5.037	13.20	9.57
29/12/2007	23:35	J46	5.981	5.010	13.02	9.45	06/01/2008	21:17	J51	5.983	5.037	13.16	9.53
29/12/2007	23:36	J46	5.981	5.010	13.00	9.43	06/01/2008	21:17	J51	5.983	5.037	13.20	9.57
29/12/2007	23:37	J46	5.981	5.010	13.00	9.43	06/01/2008	21:32	J51	5.983	5.037	13.20	9.57
29/12/2007	23:38	J46	5.981	5.010	13.02	9.45	06/01/2008	22:04	J47	5.983	5.037	13.10	9.47
29/12/2007	23:39	J46	5.981	5.010	13.00	9.43	06/01/2008	22:09	J47	5.983	5.037	13.15	9.52
29/12/2007	23:40	J46	5.981	5.010	12.99	9.42	06/01/2008	22:15	J47	5.983	5.037	13.20	9.57
29/12/2007	23:41	J46	5.981	5.010	12.98	9.41	07/01/2008	01:24	J40	5.983	5.037	13.20	9.57
29/12/2007	23:42	J46	5.981	5.010	12.99	9.42	07/01/2008	01:34	J40	5.983	5.037	13.20	9.57
29/12/2007	23:43	J46	5.981	5.010	12.97	9.40	07/01/2008	01:35	J40	5.983	5.037	13.21	9.58
29/12/2007	23:44	J46	5.981	5.010	13.00	9.43	07/01/2008	01:43	J40	5.983	5.037	13.30	9.67
29/12/2007	23:45	J46	5.981	5.010	12.99	9.42	07/01/2008	20:00	J46	5.983	5.037	13.29	9.65
29/12/2007	23:46	J46	5.981	5.010	13.00	9.43	07/01/2008	22:04	J47	5.984	5.042	13.30	9.66
29/12/2007	23:47	J46	5.981	5.010	12.98	9.41	07/01/2008	22:11	J47	5.984	5.042	13.40	9.76
29/12/2007	23:49	J46	5.981	5.010	12.98	9.41	07/01/2008	22:18	J47	5.984	5.042	13.40	9.76
29/12/2007	23:50	J46	5.981	5.010	12.99	9.42	07/01/2008	23:19	945	5.984	5.042	13.30	9.66
29/12/2007	23:51	J46	5.981	5.010	12.97	9.40	07/01/2008	23:22	945	5.984	5.042	13.30	9.66
29/12/2007	23:52	J46	5.981	5.010	12.99	9.42	07/01/2008	23:24	945	5.984	5.042	13.32	9.68
29/12/2007	23:53	J46	5.981	5.010	12.97	9.40	07/01/2008	23:25	945	5.984	5.042	13.30	9.66
29/12/2007	23:54	J46	5.981	5.010	12.97	9.40	07/01/2008	23:27	945	5.984	5.042	13.30	9.66
29/12/2007	23:55	J46	5.981	5.010	12.98	9.41	07/01/2008	23:29	945	5.984	5.042	13.40	9.76
29/12/2007	23:56	J46	5.981	5.010	12.98	9.41	08/01/2008	20:58	213	5.984	5.047	13.70	10.05
29/12/2007	23:57	J46	5.981	5.010	12.97	9.40	08/01/2008	23:05	J46	5.984	5.047	13.56	9.91
29/12/2007	23:58	J46	5.981	5.010	12.97	9.40	09/01/2008	20:05	J46	5.984	5.052	13.83	10.17
29/12/2007	23:59	J46	5.981	5.010	12.96	9.39	09/01/2008	22:37	J47	5.984	5.052	13.90	10.24
30/12/2007	00:00	J46	5.981	5.010	12.97	9.40	09/01/2008	22:41	J47	5.984	5.052	13.80	10.14
30/12/2007	00:01	J46	5.981	5.010	12.95	9.38	09/01/2008	22:44	J47	5.984	5.052	13.89	10.23
30/12/2007	00:02	J46	5.981	5.010	12.97	9.40	09/01/2008	22:55	J47	5.984	5.052	13.90	10.24
30/12/2007	00:03	J46	5.981	5.010	12.95	9.38	09/01/2008	23:55	945	5.984	5.052	13.90	10.24
30/12/2007	00:04	J46	5.981	5.010	12.96	9.39	09/01/2008	23:59	945	5.984	5.052	14.00	10.34
30/12/2007	00:05	J46	5.981	5.010	12.97	9.40	10/01/2008	00:01	945	5.984	5.052	13.99	10.33
30/12/2007	00:07	J46	5.981	5.010	12.98	9.41	10/01/2008	00:02	945	5.984	5.052	14.00	10.34
30/12/2007	00:08	J46	5.981	5.010	12.93	9.36	10/01/2008	00:10	945	5.984	5.052	14.10	10.44
30/12/2007	00:09	J46	5.981	5.010	12.96	9.39	10/01/2008	19:48	213	5.985	5.058	14.30	10.63
30/12/2007	00:10	J46	5.981	5.010	12.95	9.38	10/01/2008	19:53	213	5.985	5.058	14.30	10.63
30/12/2007	00:11	J46	5.981	5.010	12.98	9.41	10/01/2008	19:56	213	5.985	5.058	14.31	10.64
30/12/2007	00:12	J46	5.981	5.010	12.95	9.38	10/01/2008	20:04	213	5.985	5.058	14.30	10.63

[a] Observer MPC code.

Table D.2. Magnitudes in an aperture with a diameter of 10″ in 2010.

Date jj/mm/yyyy	Time hr:mn	Obs[a]	r_h (au)	Δ (au)	m_R	$m_R(1, r_h, 0)$	Date jj/mm/yyyy	Time hr:mn	Obs	r_h (au)	Δ (au)	m_R	$m_R(1, r_h, 0)$
02/04/2010	21:19	J97	6.203	5.582	15.80	11.75	25/04/2010	22:28	213	6.207	5.921	14.40	10.16
02/04/2010	21:25	J97	6.203	5.582	15.80	11.75	25/04/2010	22:51	945	6.207	5.921	14.40	10.16
02/04/2010	21:26	J97	6.203	5.582	15.80	11.75	25/04/2010	22:56	945	6.207	5.921	14.50	10.26
02/04/2010	21:31	J97	6.203	5.582	15.80	11.75	25/04/2010	23:00	945	6.207	5.921	14.40	10.16
02/04/2010	23:03	J53	6.203	5.582	16.10	12.05	25/04/2010	23:02	945	6.207	5.921	14.48	10.24
02/04/2010	23:09	J53	6.203	5.582	16.07	12.02	25/04/2010	23:04	945	6.207	5.921	14.50	10.26
02/04/2010	23:12	J53	6.203	5.582	16.10	12.05	25/04/2010	23:09	945	6.207	5.921	14.40	10.16
02/04/2010	23:14	J53	6.203	5.582	16.10	12.05	26/04/2010	22:24	945	6.207	5.921	14.61	10.37
02/04/2010	23:17	J47	6.203	5.582	16.00	11.95	26/04/2010	22:36	J38	6.207	5.921	14.85	10.61
02/04/2010	23:40	J47	6.203	5.582	15.90	11.85	27/04/2010	20:13	B20	6.208	5.937	14.68	10.43
03/04/2010	00:01	J47	6.203	5.582	15.90	11.85	27/04/2010	20:37	213	6.208	5.937	14.97	10.72
04/04/2010	19:51	213	6.198	5.283	16.10	12.16	27/04/2010	21:02	J47	6.208	5.937	14.80	10.55
04/04/2010	20:14	213	6.198	5.283	16.08	12.14	27/04/2010	21:22	J38	6.208	5.937	14.88	10.63
04/04/2010	20:19	213	6.198	5.283	16.10	12.16	28/04/2010	20:45	C12	6.208	5.953	15.21	10.96
04/04/2010	20:33	213	6.198	5.283	16.10	12.16	28/04/2010	21:59	213	6.208	5.953	15.05	10.80
04/04/2010	22:37	945	6.198	5.283	16.10	12.16	01/05/2010	21:13	J36	6.208	6.000	15.22	10.95
04/04/2010	22:41	945	6.198	5.283	16.10	12.16	04/05/2010	21:35	J40	6.209	6.065	15.59	11.29
04/04/2010	22:48	945	6.198	5.283	16.10	12.16	05/05/2010	20:35	J47	6.209	6.081	14.90	10.60
04/04/2010	22:50	945	6.198	5.283	16.10	12.16	05/05/2010	20:47	J47	6.209	6.081	14.94	10.64
04/04/2010	22:54	945	6.198	5.283	16.10	12.16	05/05/2010	20:57	J38	6.209	6.081	14.98	10.68
04/04/2010	23:03	945	6.198	5.283	16.10	12.16	05/05/2010	20:59	J38	6.209	6.081	15.00	10.70
04/04/2010	23:17	J53	6.198	5.283	16.20	12.26	05/05/2010	21:02	J38	6.209	6.081	15.00	10.70
04/04/2010	23:40	J53	6.198	5.283	16.13	12.19	05/05/2010	21:03	J47	6.209	6.081	14.90	10.60
04/04/2010	23:43	J53	6.198	5.283	16.20	12.26	05/05/2010	21:05	J38	6.209	6.081	15.00	10.70
04/04/2010	23:49	J53	6.198	5.283	16.10	12.16	05/05/2010	21:17	J40	6.209	6.081	14.88	10.58
05/04/2010	21:07	J47	6.198	5.290	16.10	12.15	06/05/2010	21:30	B74	6.209	6.097	14.83	10.52
05/04/2010	21:13	J47	6.198	5.290	16.10	12.15	07/05/2010	19:44	213	6.210	6.113	15.00	10.69
05/04/2010	21:22	J47	6.198	5.290	16.10	12.15	07/05/2010	19:53	213	6.210	6.113	15.03	10.72
05/04/2010	21:51	J51	6.198	5.290	16.10	12.15	07/05/2010	20:02	213	6.210	6.113	15.10	10.79
05/04/2010	22:10	J51	6.198	5.290	16.10	12.15	07/05/2010	21:09	J47	6.210	6.113	14.90	10.59
05/04/2010	22:30	J51	6.198	5.290	16.10	12.15	07/05/2010	21:25	J40	6.210	6.113	14.93	10.62
06/04/2010	00:20	945	6.198	5.290	16.00	12.05	07/05/2010	21:31	J47	6.210	6.113	14.94	10.63
06/04/2010	00:24	945	6.198	5.290	16.00	12.05	07/05/2010	21:32	212	6.210	6.113	15.00	10.69
06/04/2010	00:26	945	6.198	5.290	16.01	12.06	07/05/2010	21:33	J47	6.210	6.113	14.90	10.59
06/04/2010	00:28	945	6.198	5.290	16.00	12.05	07/05/2010	21:40	212	6.210	6.113	14.97	10.66
06/04/2010	00:32	945	6.198	5.290	16.00	12.05	07/05/2010	21:42	212	6.210	6.113	14.90	10.59
06/04/2010	00:36	945	6.198	5.290	16.00	12.05	07/05/2010	21:47	212	6.210	6.113	15.00	10.69
07/04/2010	22:16	J53	6.204	5.650	16.10	12.00	07/05/2010	21:51	J47	6.210	6.113	15.00	10.69
07/04/2010	22:29	J53	6.204	5.650	16.13	12.03	08/05/2010	19:45	213	6.210	6.145	15.00	10.67
07/04/2010	22:30	J53	6.204	5.650	16.10	12.00	08/05/2010	20:00	213	6.210	6.145	14.90	10.57
07/04/2010	22:44	J53	6.204	5.650	16.10	12.00	08/05/2010	20:00	213	6.210	6.145	14.96	10.63
07/04/2010	23:51	I96	6.204	5.650	16.10	12.00	08/05/2010	20:15	213	6.210	6.145	14.90	10.57
08/04/2010	00:22	I96	6.204	5.650	16.10	12.00	08/05/2010	20:23	213	6.210	6.145	14.96	10.63
08/04/2010	00:26	I96	6.204	5.650	16.13	12.03	08/05/2010	20:31	B74	6.210	6.145	14.80	10.47
08/04/2010	01:05	I96	6.204	5.650	16.20	12.10	08/05/2010	20:35	B74	6.210	6.145	14.80	10.47
08/04/2010	22:26	J53	6.204	5.650	16.10	12.00	08/05/2010	20:37	B74	6.210	6.145	14.81	10.48
08/04/2010	22:32	J53	6.204	5.650	16.20	12.10	08/05/2010	20:42	B74	6.210	6.145	14.80	10.47
08/04/2010	22:32	J53	6.204	5.650	16.24	12.14	08/05/2010	22:43	I32	6.210	6.145	14.86	10.53
08/04/2010	22:38	J53	6.204	5.650	16.30	12.20	09/05/2010	20:12	J98	6.210	6.145	15.20	10.87
09/04/2010	19:35	A06	6.205	5.679	16.10	11.99	09/05/2010	20:13	J98	6.210	6.145	15.10	10.77
09/04/2010	20:00	A06	6.205	5.679	16.11	12.00	09/05/2010	20:14	J98	6.210	6.145	15.00	10.67
09/04/2010	20:12	A06	6.205	5.679	16.10	11.99	09/05/2010	21:04	945	6.210	6.145	14.90	10.57
09/04/2010	20:39	213	6.205	5.679	16.20	12.09	09/05/2010	21:08	945	6.210	6.145	14.90	10.57
09/04/2010	20:49	213	6.205	5.679	16.19	12.08	09/05/2010	21:12	945	6.210	6.145	14.90	10.57
09/04/2010	20:49	213	6.205	5.679	16.20	12.09	09/05/2010	21:14	945	6.210	6.145	14.92	10.59
09/04/2010	20:59	213	6.205	5.679	16.20	12.09	09/05/2010	21:16	945	6.210	6.145	14.90	10.57
09/04/2010	21:06	J97	6.205	5.679	16.10	11.99	09/05/2010	21:24	945	6.210	6.145	14.90	10.57
09/04/2010	21:14	J97	6.205	5.679	16.00	11.89	10/05/2010	20:42	J47	6.210	6.161	15.10	10.77
09/04/2010	21:15	J97	6.205	5.679	16.10	11.99	10/05/2010	20:49	J47	6.210	6.161	15.10	10.77
09/04/2010	21:20	J97	6.205	5.679	16.10	11.99	10/05/2010	20:49	J47	6.210	6.161	15.14	10.81
09/04/2010	21:20	B20	6.205	5.679	16.15	12.04	10/05/2010	20:57	J47	6.210	6.161	15.20	10.87
10/04/2010	20:27	B20	6.205	5.693	16.09	11.97	11/05/2010	20:40	J47	6.210	6.161	15.40	11.07
10/04/2010	21:21	945	6.205	5.693	15.90	11.78	11/05/2010	20:54	J47	6.210	6.161	15.40	11.07
10/04/2010	21:34	945	6.205	5.693	15.80	11.68	11/05/2010	20:57	J47	6.210	6.177	15.40	11.06

Continued on next page

Date jj/mm/yyyy	Time hr:mn	Obs	r_h (au)	Δ (au)	m_R	$m_R(1, r_h, 0)$	Date jj/mm/yyyy	Time hr:mn	Obs	r_h (au)	Δ (au)	m_R	$m_R(1, r_h, 0)$
10/04/2010	21:37	945	6.205	5.693	15.86	11.74	11/05/2010	21:18	J47	6.210	6.161	15.40	11.07
10/04/2010	21:41	945	6.205	5.693	15.90	11.78	11/05/2010	22:12	J40	6.210	6.177	15.38	11.04
10/04/2010	21:46	945	6.205	5.693	15.80	11.68	13/05/2010	21:11	J38	6.211	6.210	15.60	11.25
10/04/2010	21:51	945	6.205	5.693	15.90	11.78	13/05/2010	21:14	J38	6.211	6.210	15.60	11.25
10/04/2010	22:43	J53	6.205	5.693	16.10	11.98	13/05/2010	21:18	J38	6.211	6.210	15.60	11.25
10/04/2010	22:49	J53	6.205	5.693	16.11	11.99	13/05/2010	21:19	J38	6.211	6.210	15.62	11.27
10/04/2010	22:49	J53	6.205	5.693	16.00	11.88	15/05/2010	20:58	213	6.211	6.242	16.00	11.64
10/04/2010	22:56	J53	6.205	5.693	16.20	12.08	15/05/2010	21:10	213	6.211	6.242	15.98	11.62
12/04/2010	21:06	J38	6.205	5.722	16.10	11.96	15/05/2010	21:10	213	6.211	6.242	16.00	11.64
12/04/2010	21:11	J38	6.205	5.722	16.10	11.96	15/05/2010	21:15	213	6.211	6.242	16.00	11.64
12/04/2010	21:16	J38	6.205	5.722	16.14	12.00	15/05/2010	21:25	J53	6.211	6.242	15.90	11.54
12/04/2010	21:24	J38	6.205	5.722	16.10	11.96	15/05/2010	21:27	J53	6.211	6.242	15.80	11.44
12/04/2010	22:44	J47	6.205	5.722	16.30	12.16	15/05/2010	21:27	213	6.211	6.242	15.86	11.50
12/04/2010	23:03	J47	6.205	5.722	16.30	12.16	15/05/2010	21:30	J53	6.211	6.242	15.83	11.47
12/04/2010	23:04	J47	6.205	5.722	16.31	12.17	15/05/2010	21:31	J53	6.211	6.242	15.80	11.44
12/04/2010	23:28	J47	6.205	5.722	16.30	12.16	15/05/2010	22:15	A01	6.211	6.242	15.60	11.24
14/04/2010	20:27	213	6.205	5.752	16.50	12.35	15/05/2010	22:18	A01	6.211	6.242	15.60	11.24
14/04/2010	20:32	213	6.205	5.752	16.45	12.30	15/05/2010	22:21	A01	6.211	6.242	15.58	11.22
14/04/2010	20:37	213	6.205	5.752	16.40	12.25	15/05/2010	22:29	A01	6.211	6.242	15.50	11.14
14/04/2010	20:57	J38	6.205	5.752	16.40	12.25	16/05/2010	20:18	J98	6.211	6.258	15.50	11.14
14/04/2010	21:00	J38	6.205	5.752	16.40	12.25	16/05/2010	20:20	J98	6.211	6.258	15.64	11.28
14/04/2010	21:04	J38	6.205	5.752	16.38	12.23	16/05/2010	20:22	J98	6.211	6.258	15.70	11.34
14/04/2010	21:09	J38	6.205	5.752	16.40	12.25	16/05/2010	21:41	J53	6.211	6.258	15.90	11.54
14/04/2010	21:42	J47	6.205	5.752	16.40	12.25	16/05/2010	21:43	J53	6.211	6.258	15.90	11.54
14/04/2010	21:46	J47	6.205	5.752	16.30	12.15	16/05/2010	21:45	J53	6.211	6.258	15.89	11.53
14/04/2010	21:47	J47	6.205	5.752	16.36	12.21	16/05/2010	21:49	J53	6.211	6.258	15.90	11.54
14/04/2010	21:52	J47	6.205	5.752	16.40	12.25	16/05/2010	21:57	J40	6.211	6.258	15.90	11.54
14/04/2010	23:07	945	6.205	5.752	16.10	11.95	17/05/2010	20:49	213	6.211	6.274	16.00	11.63
14/04/2010	23:12	945	6.205	5.752	16.20	12.05	17/05/2010	20:55	213	6.211	6.274	16.08	11.71
14/04/2010	23:17	945	6.205	5.752	16.10	11.95	17/05/2010	21:00	213	6.211	6.274	16.10	11.73
14/04/2010	23:19	945	6.205	5.752	16.18	12.03	17/05/2010	21:05	213	6.211	6.274	16.10	11.73
14/04/2010	23:21	945	6.205	5.752	16.20	12.05	17/05/2010	21:32	J38	6.211	6.274	15.90	11.53
14/04/2010	23:25	945	6.205	5.752	16.10	11.95	17/05/2010	21:36	J38	6.211	6.274	15.97	11.60
16/04/2010	19:22	A06	6.206	5.782	12.80	8.63	17/05/2010	21:38	J38	6.211	6.274	16.00	11.63
16/04/2010	19:45	A06	6.206	5.782	12.80	8.63	17/05/2010	21:44	J38	6.211	6.274	16.00	11.63
16/04/2010	19:51	A06	6.206	5.782	12.90	8.73	18/05/2010	21:04	J40	6.212	6.289	16.11	11.74
16/04/2010	20:08	A06	6.206	5.782	12.90	8.73	18/05/2010	21:31	945	6.212	6.289	16.00	11.63
16/04/2010	20:28	213	6.206	5.782	12.70	8.53	18/05/2010	21:35	945	6.212	6.289	15.90	11.53
16/04/2010	20:35	A06	6.206	5.782	12.80	8.63	18/05/2010	21:39	945	6.212	6.289	16.00	11.63
16/04/2010	20:39	C12	6.206	5.782	12.80	8.63	18/05/2010	21:41	945	6.212	6.289	15.92	11.55
16/04/2010	20:42	213	6.206	5.782	12.80	8.63	18/05/2010	21:47	945	6.212	6.289	15.90	11.53
16/04/2010	20:42	213	6.206	5.782	12.76	8.59	18/05/2010	21:54	945	6.212	6.289	16.00	11.63
16/04/2010	20:43	C12	6.206	5.782	12.80	8.63	19/05/2010	21:06	B74	6.212	6.305	15.70	11.32
16/04/2010	20:45	C12	6.206	5.782	12.82	8.65	19/05/2010	21:39	J38	6.212	6.305	15.89	11.51
16/04/2010	20:47	C12	6.206	5.782	12.80	8.63	19/05/2010	22:57	J40	6.212	6.305	16.00	11.62
16/04/2010	20:49	213	6.206	5.782	12.80	8.63	21/05/2010	20:37	B20	6.212	6.337	15.60	11.21
16/04/2010	20:51	C12	6.206	5.782	12.80	8.63	21/05/2010	20:42	A06	6.212	6.337	15.60	11.21
16/04/2010	20:56	J38	6.206	5.782	12.80	8.63	21/05/2010	20:58	A06	6.212	6.337	15.60	11.21
16/04/2010	21:00	J38	6.206	5.782	12.82	8.65	21/05/2010	21:01	A06	6.212	6.337	15.64	11.25
16/04/2010	21:01	J38	6.206	5.782	12.80	8.63	21/05/2010	21:14	A06	6.212	6.337	15.60	11.21
16/04/2010	21:04	J38	6.206	5.782	12.80	8.63	21/05/2010	21:23	J38	6.212	6.337	15.40	11.01
17/04/2010	20:32	C12	6.206	5.797	12.90	8.72	21/05/2010	21:26	J38	6.212	6.337	15.50	11.11
17/04/2010	20:37	C12	6.206	5.797	12.90	8.72	21/05/2010	21:30	J38	6.212	6.337	15.48	11.09
17/04/2010	20:38	C12	6.206	5.797	12.92	8.74	21/05/2010	21:32	J38	6.212	6.337	15.50	11.11
17/04/2010	20:41	C12	6.206	5.797	12.90	8.72	22/05/2010	20:15	213	6.212	6.353	15.90	11.51
17/04/2010	20:47	B74	6.206	5.782	12.90	8.73	22/05/2010	20:25	213	6.212	6.353	15.80	11.41
17/04/2010	20:49	B74	6.206	5.782	12.88	8.71	22/05/2010	20:37	213	6.212	6.353	15.83	11.44
17/04/2010	20:49	B74	6.206	5.782	12.90	8.73	22/05/2010	20:57	213	6.212	6.353	15.70	11.31
17/04/2010	20:50	B74	6.206	5.782	12.90	8.73	22/05/2010	21:27	945	6.212	6.353	15.60	11.21
17/04/2010	20:56	213	6.206	5.797	12.90	8.72	22/05/2010	21:34	945	6.212	6.353	15.70	11.31
17/04/2010	21:01	213	6.206	5.797	12.90	8.72	22/05/2010	21:38	945	6.212	6.353	15.60	11.21
17/04/2010	21:01	213	6.206	5.797	12.90	8.72	22/05/2010	21:40	945	6.212	6.353	15.62	11.23
17/04/2010	21:06	213	6.206	5.797	12.90	8.72	22/05/2010	21:43	945	6.212	6.353	15.60	11.21
17/04/2010	22:03	J47	6.206	5.797	12.90	8.72	22/05/2010	21:50	J38	6.212	6.353	15.45	11.06
17/04/2010	22:07	J47	6.206	5.797	12.90	8.72	22/05/2010	21:52	945	6.212	6.353	15.60	11.21
17/04/2010	22:14	J47	6.206	5.782	12.89	8.72	22/05/2010	21:55	J38	6.212	6.353	15.50	11.11

Date jj/mm/yyyy	Time hr:mn	Obs	r_h (au)	Δ (au)	m_R	$m_R(1, r_h, 0)$	Date jj/mm/yyyy	Time hr:mn	Obs	r_h (au)	Δ (au)	m_R	$m_R(1, r_h, 0)$
17/04/2010	22:14	J47	6.206	5.797	12.90	8.72	22/05/2010	21:58	J38	6.212	6.353	15.40	11.01
17/04/2010	22:17	J38	6.206	5.782	12.90	8.73	23/05/2010	21:26	945	6.212	6.368	15.90	11.50
17/04/2010	22:20	J47	6.206	5.797	12.90	8.72	23/05/2010	21:42	945	6.212	6.368	15.80	11.40
17/04/2010	22:23	J38	6.206	5.782	12.80	8.63	23/05/2010	21:51	945	6.212	6.368	15.90	11.50
17/04/2010	22:24	J38	6.206	5.782	12.88	8.71	23/05/2010	21:57	945	6.212	6.368	15.80	11.40
17/04/2010	22:24	J47	6.206	5.797	12.90	8.72	24/05/2010	21:02	213	6.213	6.384	14.90	10.50
17/04/2010	22:28	J38	6.206	5.782	12.90	8.73	24/05/2010	21:06	213	6.213	6.384	14.85	10.45
17/04/2010	23:15	J24	6.206	5.782	12.85	8.68	24/05/2010	21:10	213	6.213	6.384	14.80	10.40
18/04/2010	19:29	A06	6.206	5.812	13.15	8.96	24/05/2010	21:47	213	6.213	6.384	14.80	10.40
18/04/2010	20:31	213	6.206	5.812	13.20	9.01	24/05/2010	21:50	213	6.213	6.384	14.80	10.40
18/04/2010	20:42	213	6.206	5.812	13.17	8.98	24/05/2010	21:52	213	6.213	6.384	14.80	10.40
18/04/2010	20:45	213	6.206	5.812	13.20	9.01	25/05/2010	20:08	213	6.213	6.400	14.80	10.40
18/04/2010	20:54	213	6.206	5.812	13.20	9.01	25/05/2010	20:14	213	6.213	6.400	14.80	10.40
18/04/2010	21:15	213	6.206	5.812	13.14	8.95	25/05/2010	20:14	213	6.213	6.400	14.81	10.41
18/04/2010	22:18	A02	6.206	5.812	13.10	8.91	25/05/2010	20:15	B74	6.213	6.400	14.80	10.40
18/04/2010	22:19	A02	6.206	5.812	13.10	8.91	25/05/2010	20:27	B74	6.213	6.400	14.72	10.32
18/04/2010	22:23	A02	6.206	5.812	13.10	8.91	25/05/2010	20:29	B74	6.213	6.400	14.70	10.30
18/04/2010	23:08	A02	6.206	5.812	13.10	8.91	25/05/2010	20:30	213	6.213	6.400	14.70	10.30
18/04/2010	23:11	A02	6.206	5.812	13.10	8.91	25/05/2010	20:37	213	6.213	6.400	14.80	10.40
18/04/2010	23:14	A02	6.206	5.812	13.10	8.91	25/05/2010	20:37	B74	6.213	6.400	14.70	10.30
18/04/2010	23:17	A02	6.206	5.812	13.10	8.91	25/05/2010	20:51	213	6.213	6.400	14.80	10.40
19/04/2010	20:54	213	6.206	5.827	13.30	9.11	25/05/2010	21:06	J30	6.213	6.400	14.96	10.56
19/04/2010	21:02	213	6.206	5.827	13.36	9.17	25/05/2010	21:10	J30	6.213	6.400	14.87	10.47
19/04/2010	21:05	213	6.206	5.827	13.40	9.21	25/05/2010	21:10	J30	6.213	6.400	14.80	10.40
19/04/2010	21:10	213	6.206	5.827	13.40	9.21	25/05/2010	21:14	J30	6.213	6.400	14.86	10.46
19/04/2010	21:19	213	6.206	5.827	13.38	9.19	26/05/2010	21:10	J30	6.213	6.415	14.94	10.53
20/04/2010	21:38	C12	6.207	5.843	13.90	9.70	26/05/2010	21:14	J30	6.213	6.415	14.81	10.40
20/04/2010	21:47	C12	6.207	5.843	13.80	9.60	26/05/2010	21:14	J30	6.213	6.415	14.64	10.23
20/04/2010	21:48	C12	6.207	5.843	13.85	9.65	26/05/2010	21:18	J30	6.213	6.415	14.84	10.43
20/04/2010	21:51	C12	6.207	5.843	13.90	9.70	29/05/2010	20:58	J30	6.213	6.461	15.51	11.09
20/04/2010	21:58	C12	6.207	5.843	13.90	9.70	29/05/2010	21:03	J30	6.213	6.461	15.22	10.80
20/04/2010	22:14	B20	6.207	5.843	13.80	9.60	29/05/2010	21:03	J30	6.213	6.461	15.28	10.86
20/04/2010	22:18	945	6.207	5.843	13.60	9.40	29/05/2010	21:08	J30	6.213	6.461	15.12	10.70
20/04/2010	22:23	945	6.207	5.843	13.60	9.40	30/05/2010	20:52	B74	6.214	6.476	15.50	11.08
20/04/2010	22:25	945	6.207	5.843	13.59	9.39	30/05/2010	20:55	B74	6.214	6.476	15.60	11.18
20/04/2010	22:28	B20	6.207	5.843	13.78	9.58	30/05/2010	20:55	B74	6.214	6.476	15.57	11.15
20/04/2010	22:28	945	6.207	5.843	13.60	9.40	30/05/2010	21:02	J40	6.214	6.476	15.67	11.25
20/04/2010	22:31	945	6.207	5.843	13.60	9.40	30/05/2010	21:04	B74	6.214	6.476	15.60	11.18
20/04/2010	22:40	945	6.207	5.843	13.60	9.40	30/05/2010	21:15	213	6.214	6.476	15.60	11.18
20/04/2010	22:41	B20	6.207	5.843	13.70	9.50	30/05/2010	21:19	213	6.214	6.476	15.63	11.21
21/04/2010	22:57	J47	6.207	5.858	14.00	9.79	30/05/2010	21:19	213	6.214	6.476	15.70	11.28
21/04/2010	23:20	J47	6.207	5.858	14.03	9.82	30/05/2010	21:24	213	6.214	6.476	15.60	11.18
21/04/2010	23:29	J47	6.207	5.858	14.10	9.89	02/06/2010	20:36	B74	6.214	6.522	15.50	11.05
21/04/2010	23:36	J47	6.207	5.858	14.00	9.79	03/06/2010	20:34	B74	6.209	6.049	15.70	11.41
23/04/2010	20:10	I99	6.207	5.890	13.90	9.68	03/06/2010	20:41	B74	6.209	6.049	15.80	11.51
23/04/2010	20:14	I99	6.207	5.890	13.90	9.68	03/06/2010	20:46	B74	6.209	6.049	15.70	11.41
23/04/2010	20:21	I99	6.207	5.890	13.91	9.69	03/06/2010	20:54	B74	6.209	6.049	15.70	11.41
23/04/2010	20:21	J47	6.207	5.890	14.00	9.78	03/06/2010	21:08	J53	6.209	6.049	15.80	11.51
23/04/2010	20:23	I99	6.207	5.890	13.90	9.68	03/06/2010	21:13	J53	6.209	6.049	15.80	11.51
23/04/2010	20:32	I99	6.207	5.890	13.90	9.68	03/06/2010	21:24	J53	6.209	6.049	15.75	11.46
23/04/2010	20:39	J47	6.207	5.890	14.00	9.78	03/06/2010	21:24	945	6.209	6.049	15.70	11.41
23/04/2010	20:59	J47	6.207	5.890	14.04	9.82	03/06/2010	21:30	945	6.209	6.049	15.70	11.41
23/04/2010	21:18	J47	6.207	5.890	14.10	9.88	03/06/2010	21:34	945	6.209	6.049	15.74	11.45
23/04/2010	21:38	J47	6.207	5.890	14.00	9.78	03/06/2010	21:36	945	6.209	6.049	15.80	11.51
24/04/2010	21:12	J51	6.207	5.905	14.30	10.07	03/06/2010	21:38	J53	6.209	6.049	15.70	11.41
24/04/2010	21:23	J51	6.207	5.905	14.25	10.02	03/06/2010	21:44	J38	6.209	6.049	15.80	11.51
24/04/2010	21:36	J51	6.207	5.905	14.30	10.07	03/06/2010	21:45	945	6.209	6.049	15.80	11.51
25/04/2010	21:00	J51	6.207	5.921	14.40	10.16	03/06/2010	21:45	J38	6.209	6.049	15.78	11.49
25/04/2010	21:15	J51	6.207	5.921	14.43	10.19	03/06/2010	21:47	J38	6.209	6.049	15.80	11.51
25/04/2010	21:30	J51	6.207	5.921	14.40	10.16	03/06/2010	21:51	945	6.209	6.049	15.80	11.51
25/04/2010	22:17	213	6.207	5.921	14.40	10.16	03/06/2010	21:53	J38	6.209	6.049	15.80	11.51
25/04/2010	22:23	213	6.207	5.921	14.42	10.18	04/06/2010	20:54	B74	6.215	6.551	15.80	11.34
25/04/2010	22:23	213	6.207	5.921	14.40	10.16	05/06/2010	20:36	213	6.215	6.566	16.06	11.59

[a] Observer MPC code.